Environmental Modelling & Software 66 (2015) 131–152

Contents lists available at ScienceDirect

Environmental Modelling & Software

journal homepage: www.elsevier.com/locate/envsoft

An efficient unstructured MUSCL scheme for solving the 2D shallow water equations

Jingming Hou [a], Qiuhua Liang [a, *], Hongbin Zhang [a], Reinhard Hinkelmann [b]

[a] School of Civil Engineering & Geosciences, Newcastle University, Newcastle upon Tyne, NE1 7RU, UK
[b] Department of Civil Engineering, Technische Universität Berlin, TIB 1-B14, Gustav-Meyer-Allee 25, 13355, Berlin, Germany

ARTICLE INFO

Article history:
Received 25 September 2014
Received in revised form
8 December 2014
Accepted 9 December 2014
Available online 23 January 2015

Keywords:
MUSCL scheme
Shallow water equations
Unstructured grids
Finite volume method
Godunov-type model

ABSTRACT

The aim of this paper is to present a novel monotone upstream scheme for conservation law (MUSCL) on unstructured grids. The novel edge-based MUSCL scheme is devised to construct the required values at the midpoint of cell edges in a more straightforward and effective way compared to other conventional approaches, by making better use of the geometrical property of the triangular grids. The scheme is incorporated into a two-dimensional (2D) cell-centered Godunov-type finite volume model as proposed in Hou et al. (2013a,c) to solve the shallow water equations (SWEs). The MUSCL scheme renders the model to preserve the well-balanced property and achieve high accuracy and efficiency for shallow flow simulations over uneven terrains. Furthermore, the scheme is directly applicable to all triangular grids. Application to several numerical experiments verifies the efficiency and robustness of the current new MUSCL scheme.

1. Introduction

Two-dimensional (2D) shallow water models based on hydrostatic pressure assumption have been used to simulate a wide range of surface environmental flows including dam- or dike-break induced flood events (Viero et al., 2013; Wang et al., 2011), urban flood inundations (Hunter et al., 2007; Liang, 2010), rainfall-runoff processes (Esteves et al., 2000; Simons et al., 2014), tidal hydrodynamics and ocean tsunami hazards (Sugawara and Goto, 2012; Pelling et al., 2013), water quality and fluvial morphology (Kneis et al., 2009; Cao et al., 2006), hurricane induced storm surges (Akbar and Aliabadi, 2013), and even gravity currents (La Rocca et al., 2008), among many others. These applications may involve numerical calculation of very complex flow hydrodynamics such as shock-type flow discontinuities, transcritical flows, wetting and drying over irregular topography. A robust numerical scheme is required in order to produce accurate and stable numerical solutions for these applications.

Allowing automatic shock-capturing when computing all of the aforementioned complex flow hydrodynamics, Godunov-type finite volume schemes have been widely used to solve the shallow water equations (SWEs) over the last two to three decades (Anastasiou and Chan, 1997; Chippada et al., 1998; Yoon and Kang, 2004; Liang and Borthwick, 2009; Liang and Marche, 2009; Liang, 2010; Wang et al., 2011; Bradford and Sanders, 2002, 2005; Begnudelli and Sanders, 2006, 2007; Begnudelli et al., 2008; Sanders et al., 2010; Song et al., 2011b,a; Simons et al., 2011; Delis et al., 2008, 2011; Delis and Nikolos, 2013; Gallardo et al., 2007; George, 2010; Loukili and Soulaimani, 2007; Murillo et al., 2007; Skoula et al., 2006; Toro, 2009; Zhou et al., 2001, 2004; Murillo et al., 2006, 2008, 2009; Murillo and Garcia-Navarro, 2011; Benkhaldoun et al., 2010b,a; Zokagoa and Soulaimani, 2010; Hou et al., 2013a,c,b). For most of the applications, first-order finite volume schemes may give rise to unacceptable numerical diffusion and hence poor numerical solutions, especially for flows containing discontinuities, e.g. tsunami and dam-break waves. It is therefore necessary to develop second- or higher-order schemes to predict more accurately the shallow flows. As an effective second-order scheme, the monotone upstream scheme for conservation law (MUSCL) (van Leer, 1979) has been widely recognized and applied in solving the SWEs within the framework of finite volume Godunov-type schemes (Benkhaldoun et al., 2007; Barth and Jespersen, 1989; Hubbard, 1999; Begnudelli and Sanders, 2006, 2007; Begnudelli et al., 2008; Song et al., 2011b,a; Jawahar and Kamath, 2000; Yoon and Kang, 2004; Simões, 2011; Canestrelli et al., 2012; Hou et al., 2013c,b,a). This technique is able to substantially reduce numerical diffusion without causing unphysical

* Corresponding author.
E-mail addresses: jingming.hou@ncl.ac.uk (J. Hou), qiuhua.liang@ncl.ac.uk (Q. Liang), h.zhang3@ncl.ac.uk (H. Zhang), reinhard.hinkelmann@wahyd.tu-berlin.de (R. Hinkelmann).

http://dx.doi.org/10.1016/j.envsoft.2014.12.007

oscillations, by means of linearly reconstructing the values of flow variables within a cell or at cell interfaces. The MUSCL scheme was originally developed by van Leer (1979) for uniform grids, but substantial research effort has been devoted to extend its application on unstructured grids to allow better representation of complex domain geometries for real-world applications.

Two-dimensional unstructured MUSCL schemes may be generally classified into two categories according to the way the values of flow variables are reconstructed within a cell, i.e. cell-based and edge-based MUSCL schemes, which are also referred to as monoslope and multislope MUSCL schemes, respectively (Buffard and Clain, 2010). The cell-based MUSCL schemes use unique limited gradients of variables to reconstruct the required values at edges. A number of cell-based MUSCL schemes have been derived for unstructured grids. Being the most efficient cell-based MUSCL scheme, the limited central difference scheme (LCD) has been widely reported for solving the SWEs on unstructured grids (Hubbard, 1999; Begnudelli and Sanders, 2006, 2007; Begnudelli et al., 2008; Song et al., 2011b,a). However, this scheme is known to suffer from excessive numerical diffusion (Hubbard, 1999). A more accurate scheme was developed by Barth and Jespersen (1989), which satisfied monotonicity and was adopted by Anastasiou and Chan (1997) in their shallow water flow model. As the limiting function of Barth and Jespersen (1989) is not differentiable and likely to cause numerical instabilities near to the solution regions with constant variables, the scheme fails to provide converged solution to steady state (Venkatakrishnan, 1995; Jawahar and Kamath, 2000; Venkatakrishnan et al., 2003). To resolve the convergence problem, Venkatakrishnan (1995) devised a modified limiter which was applied by Simões (2011) to simulate shallow water flows. The schemes of Barth and Jespersen (1989) and Venkatakrishnan (1995) were incorporated into the multi-dimensional limiting process (MLP) by Park et al. (2010) to achieve a higher accuracy. The MLP based on Barth and Jespersen's limiting scheme was adopted in Canestrelli et al. (2012) to solve the SWEs. In spite of the increased accuracy, MLP requires a much wider stencil of cells and a more complicated solution procedure and hence is computationally more demanding. It should be noted that the above list of references covers only a small number of cell-based MUSCL schemes reported in literature and it is by no means exhaustive.

Unlike the cell-based MUSCL schemes that provide piecewise linear gradients at a cell, the edge-based MUSCL schemes compute the edge values by limiting 1D slopes at each edge of a cell (Buffard and Clain, 2010; Delis and Nikolos, 2013). They may not give linear functions at each cell to preserve the mean values in the cell under consideration (Buffard and Clain, 2010; Delis and Nikolos, 2013). However, it does not affect the accuracy of finite volume method because its kernel lies in computing the fluxes at the cell edges instead of the shape of the reconstructed functions at the cells (Buffard and Clain, 2010). The limiting procedure for edge-based MUSCL schemes is carried out in the same loop of computing the fluxes over all edges of a cell. This eliminates the need of an additional loop as required for cell-based MUSCL schemes for selecting the best limiter of all faces. Hence the number of times that the limiter is invoked is largely reduced (Aftosmis et al., 1994, 1995; Delis and Nikolos, 2013; Hou et al., 2013a). Therefore, the edge-based MUSCL schemes are computationally more efficient and have been employed broadly by model developers for solving the SWEs on unstructured grids (Audusse and Bristeau, 2005; Benkhaldoun et al., 2007, 2010b; Nikolos and Delis, 2009; Delis et al., 2011; Delis and Nikolos, 2013; Hou et al., 2013a,c; Simons et al., 2014). As a simple edge-based MUSCL approach, the minmod scheme that essentially selects the smaller slope between the two alternatives has been widely implemented in unstructured SWE models due to its simple formulation and superior numerical stability (Skoula et al., 2006; Benkhaldoun et al., 2007). However, it may sometimes lead to unacceptable numerical diffusion and gives the lowest order of accuracy among all MUSCL schemes. Delis et al. (2011) developed a more accurate scheme to compute the values at point D (the intersection of the edge under consideration and the line connecting two adjacent cell centroids, see Fig. 1). Another recent technique to evaluate flow information at D was presented in Kong et al. (2013). Since D does not always coincide with the midpoint M of the edge where fluxes are evaluated (Fig. 1), this type of techniques may result in a loss of accuracy on poorly connected grids (Buffard and Clain, 2010; Delis et al., 2011; Delis and Nikolos, 2013).

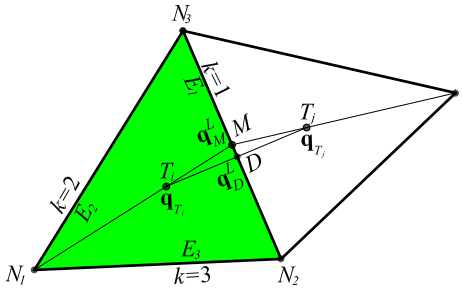

Fig. 1. Evaluating edge values (T denotes cells, E represents edges and N depicts nodes).

The reduced solution accuracy may be largely avoided by using extrapolated flow values at M to calculate the fluxes and the slope source terms (Delis et al., 2011; Buffard and Clain, 2010). The technique proposed in Buffard and Clain (2010) calculates the values at M by constructing the slopes from the cell center to point M based on those from the cell center to point D. But this may affect the computational efficiency of the overall edge-based MUSCL scheme, as a result of a more complex reconstruction procedure. Delis et al. (2011) used unlimited gradients to compute the required values at M and so the monotonicity is not rigorously guaranteed. To increase numerical stability, a new approach was reported by Delis and Nikolos (2013) to limit the slope along $\overline{DM}$ (Fig. 1). This technique prevents the potential numerical oscillations but may also lead to increased computational cost due to the necessity of involving a much wider stencil of cells on calculation. Based on the technique of Delis et al. (2011), Hou et al. (2013a) proposed a more efficient method to prevent possible local extreme when extrapolating flow variables from D to M. As demonstrated by Hou et al. (2013a), this improved scheme provides satisfactory numerical solutions for complex flows involving wetting and dying over complex terrains. However, the method is still not entirely straightforward since two steps are required to compute the values at M (firstly the values at D are computed and then they are used to extrapolate the values at M).

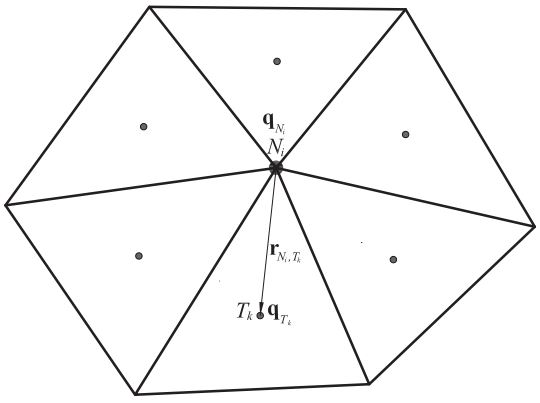

Fig. 2. Evaluating nodal values.

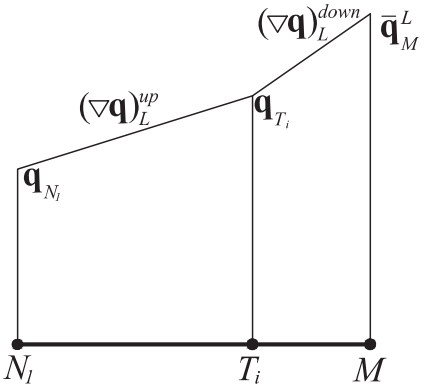

Fig. 3. Upstream and downstream slopes used for slope-limiting at the first edge of the cell under consideration (Fig. 1).

In this work, a novel 2D edge-based MUSCL scheme for triangular grids is presented to extrapolate the required values at M directly from the cell center. This scheme is devised to be more efficient but maintains the same or slightly higher numerical accuracy as the one reported in Hou et al. (2013a). The improved scheme is incorporated into a 2D Godunov-type cell-centered finite volume model to solve the SWEs in this work. The reconstructed values at the midpoints of the cell edges are modified by a non-negative water depth reconstruction (Hou et al., 2013c) that preserves the well-balanced solution or so-called conservation property (C-property) (Greenberg and Leroux, 1996). These reconstructed values are then employed to compute the fluxes using the Harten, Lax and van Leer approximate Riemann solver with the contact wave restored (HLLC) and to evaluate the slope source terms. The splitting point-implicit method proposed in Bussing and Murmant (1988) is adopted to discretize the friction source terms. To update the flow variables to a new time level, the two-stage explicit Runge–Kutta approach is applied (Hubbard, 1999; Song et al., 2011a). Implemented with the new MUSCL scheme, the current model is able to achieve second-order accuracy, converge to steady state and predict complex flow hydrodynamics that involves moving wet-dry fronts over uneven topography in an efficient way.

The remainder of the paper is organized as follows: Section 2 introduces the governing equations; Section 3 presents the novel 2D edge-based MUSCL scheme and the overall shallow flow model; Section 4 validates the model by applying it to simulate several benchmark tests; and finally brief conclusions are drawn in Section 5.

2. Governing equations

The SWEs are derived from the conservation of mass and momentum by assuming hydrostatic pressure distribution. In a vector form, the conservation law of the 2D SWEs can be written as,

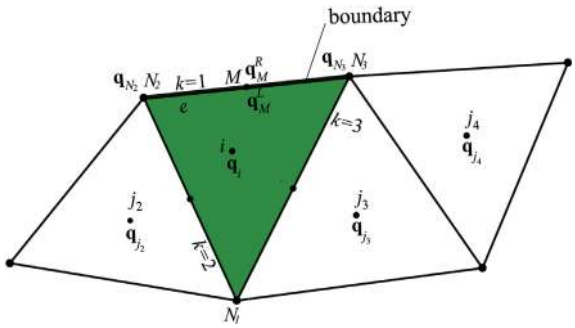

Fig. 4. Notation of variables at a triangular boundary cell.

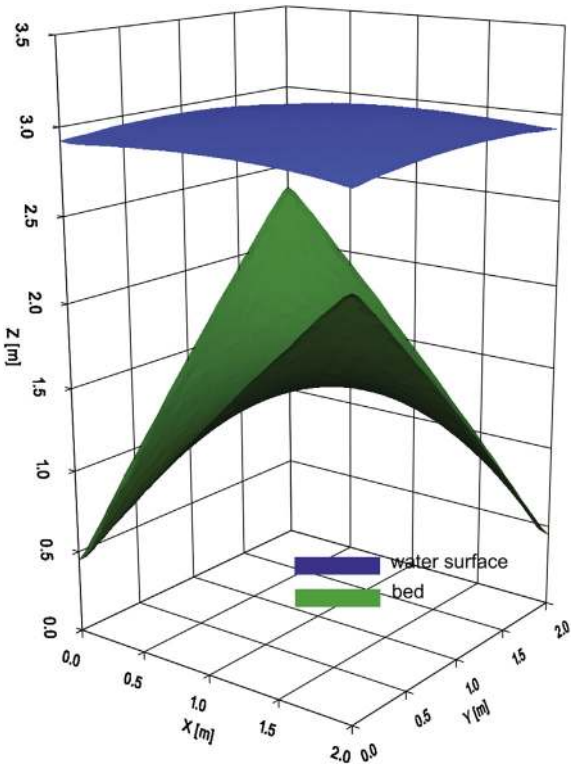

Fig. 5. Steady flow over uneven bed: analytical water level and bed.

$$\frac{\partial \mathbf{q}}{\partial t}+\frac{\partial \mathbf{f}}{\partial x}+\frac{\partial \mathbf{g}}{\partial y}=\mathbf{S}, \tag{1}$$

$$\mathbf{q}=\begin{bmatrix} h \\ q_x \\ q_y \end{bmatrix}, \mathbf{f}=\begin{bmatrix} q_x \\ uq_x+gh^2/2 \\ uq_y \end{bmatrix}, \mathbf{g}=\begin{bmatrix} q_y \\ vq_x \\ vq_y+gh^2/2 \end{bmatrix},$$
$$\mathbf{S}=\mathbf{S}_b+\mathbf{S}_f=\begin{bmatrix} 0 \\ -gh\partial z_b/\partial x \\ -gh\partial z_b/\partial y \end{bmatrix}+\begin{bmatrix} 0 \\ -C_f u\sqrt{u^2+v^2} \\ -C_f v\sqrt{u^2+v^2} \end{bmatrix}, \tag{2}$$

where t represents the time; x and y are the Cartesian coordinates; $\mathbf{q}$ denotes the vector of conserved flow variables consisting of h, $q_x=uh$ and $q_y=vh$, i.e. the water depth, unit-width discharges in the x- and y-direction, respectively; u and v are the depth-averaged velocity components in the x- and y-direction; $\mathbf{f}$ and $\mathbf{g}$ are the flux vectors in the two Cartesian directions; $\mathbf{S}$ is the source vector that may be further subdivided into the slope source terms $\mathbf{S}_b$ and friction source terms $\mathbf{S}_f$; z_b represents the bed elevation; C_f is the bed roughness coefficient that is generally computed by $gn^2/h^{1/3}$ with n being the Manning coefficient. Moreover, the water level $\eta=h+z_b$ is also used in the numerical scheme adopted in this work.

3. Numerical methods

This section describes the numerical model for solving the SWEs within the framework of an unstructured cell-centered Godunov-type finite volume scheme. The SWEs are discretized into algebraic equations by the finite volume method. The fluxes of mass and momentum are computed by the HLLC approximate Riemann solver (Toro et al., 1994). The slope source terms are evaluated by the slope flux method as proposed in Hou et al. (2013c). The friction source

terms are calculated by the splitting point-implicit method as presented in Liang and Marche (2009). The two-stage explicit Runge–Kutta approach is applied to update the flow variables to a new time level. When computing the fluxes and the slope source terms, the values at the midpoints of the cell edges are required. These values are evaluated by a novel 2D edge-based MUSCL scheme which is the main focus of this work and is presented in detail in Subsection 3.3.

3.1. Finite volume method on unstructured grids

The SWEs (1) can be integrated over a cell as

$$\int_{\Omega} \frac{\partial \mathbf{q}}{\partial t} d\Omega + \int_{\Omega} \left(\frac{\partial \mathbf{f}}{\partial x} + \frac{\partial \mathbf{g}}{\partial y} \right) d\Omega = \int_{\Omega} \mathbf{S} d\Omega, \tag{3}$$

where Ω denotes the volume of the cell i. Using the divergence theorem, Equation (3) may be transformed into

$$\int_{\Omega} \frac{\partial \mathbf{q}}{\partial t} d\Omega + \oint_{\Gamma} \mathbf{F}(\mathbf{q}) \cdot \mathbf{n} d\Gamma = \int_{\Omega} \left(\mathbf{S}_b + \mathbf{S}_f \right) d\Omega, \tag{4}$$

herein, Γ is the boundary of the cell under consideration; $\mathbf{n} = (n_x, n_y)^T$ represents the unit outward vector normal to the boundary being considered; the outward flux $\mathbf{F}(\mathbf{q}) \cdot \mathbf{n}$ at the boundary is defined as

$$\mathbf{F}(\mathbf{q}) \cdot \mathbf{n} = (\mathbf{f} n_x + \mathbf{g} n_y) = \begin{bmatrix} q_x n_x + q_y n_y \\ \left(u q_x + g h^2 / 2 \right) n_x + v q_x n_y \\ u q_y n_x + \left(v q_y + g h^2 / 2 \right) n_y \end{bmatrix}. \tag{5}$$

For a triangular cell, the circular integral for $\mathbf{F}(\mathbf{q}) \cdot \mathbf{n}$ over the boundary can be rewritten as

$$\oint_{\Gamma} \mathbf{F}(\mathbf{q}) \cdot \mathbf{n} d\Gamma = \sum_{k=1}^{3} \mathbf{F}_k(\mathbf{q}) \cdot \mathbf{n}_k l_k, \tag{6}$$

where k and l are the index and length of the edges of cell i.

3.2. Time updating

The two-stage explicit Runge-Kutta time-integration scheme (Hubbard, 1999; Liang and Borthwick, 2009; Liang and Marche,

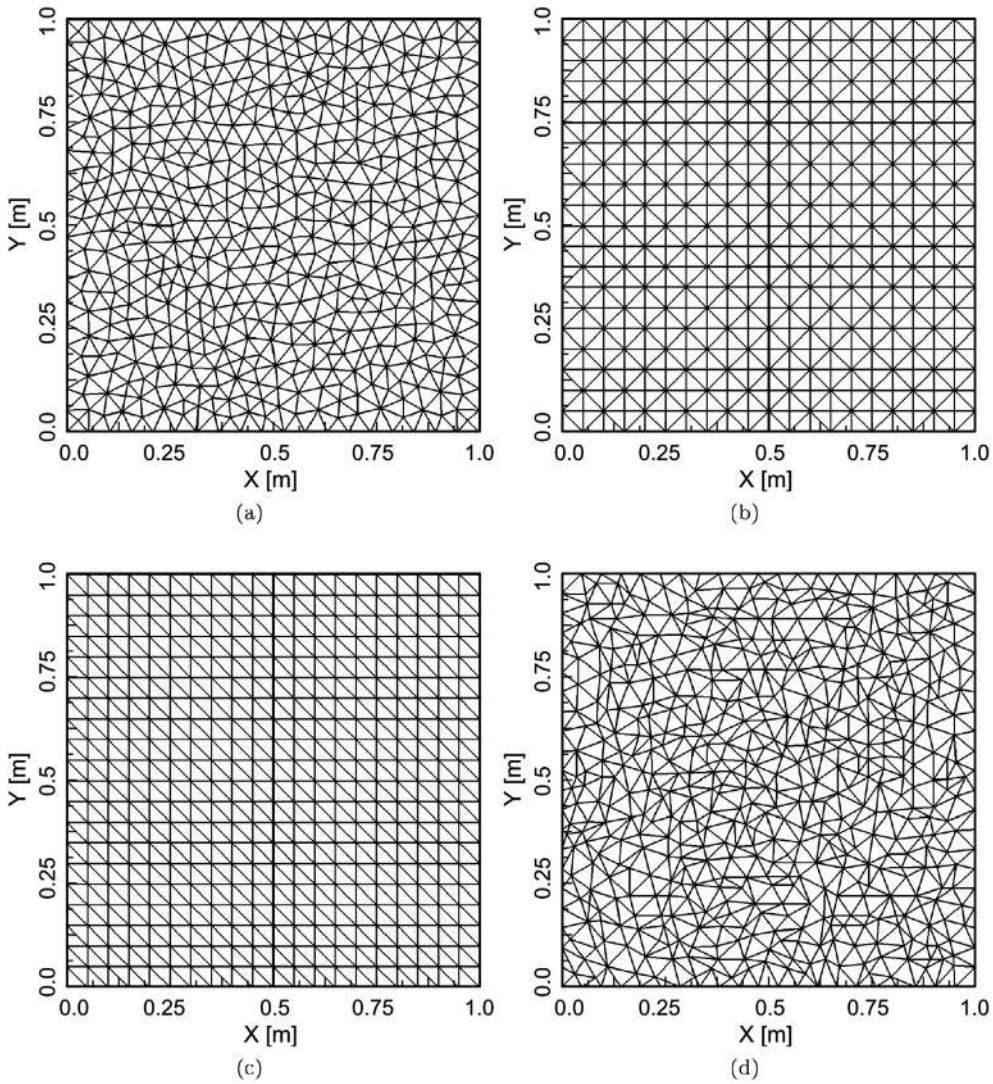

Fig. 6. Common triangular grids: (a) Delaunay grid (type A), (b) Scottish grid (type B), (c) diagonal grid (type C), (d) distorted grid (type D) (Buffard and Clain, 2010; Hou et al., 2013c).

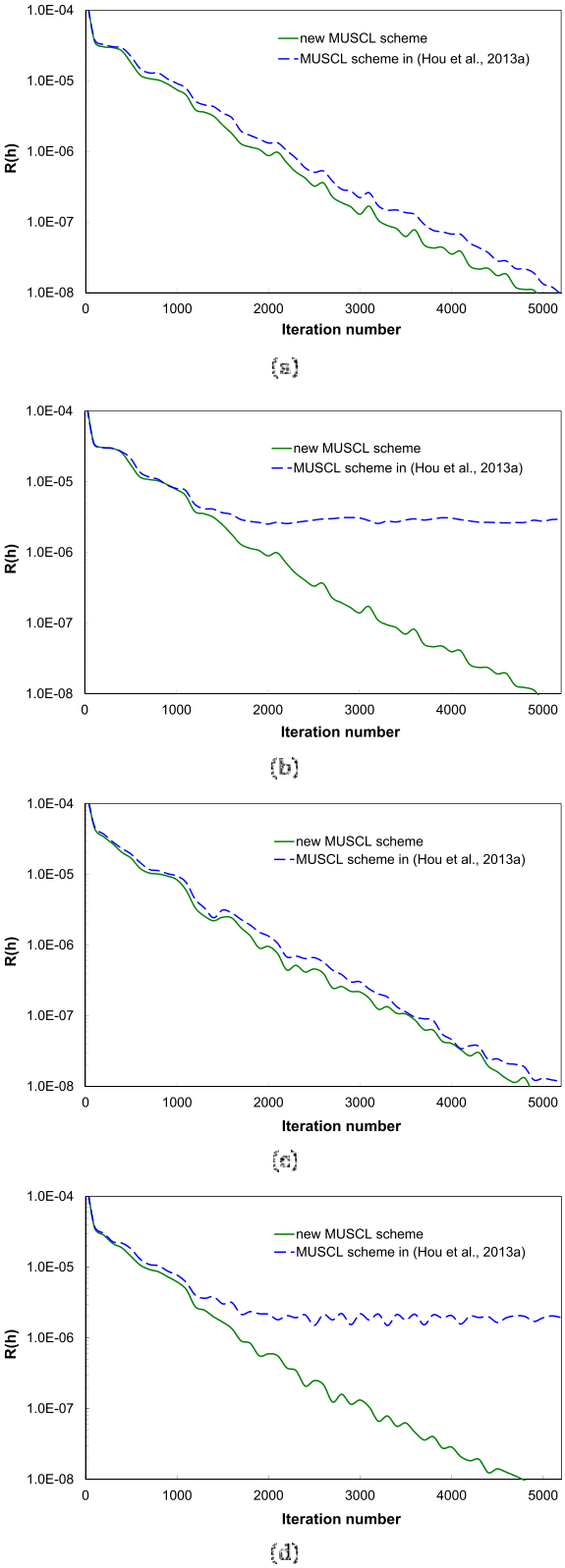

Fig. 7. Steady flow over uneven bed: relative root mean square errors for h on different grids: (a) type A, (b) type B, (c) type C, (d) type D.

2009; Song et al., 2011b; Liang, 2010; Wang et al., 2011; Song et al., 2011a) is adopted to compute the flow variables at the new time level. At cell T_i that is under consideration, the flow variables at the new time level are obtained by

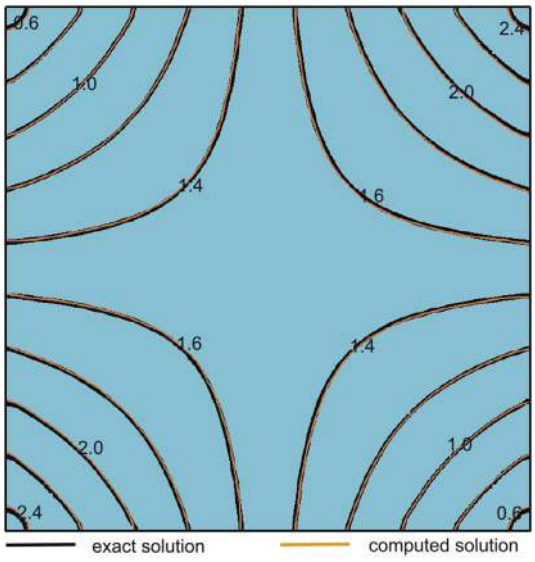

Fig. 8. Steady flow over uneven bed: water depth contours computed by the new MUSCL scheme on the Delaunay grid (m).

$$\mathbf{q}_{T_i}^{n+1} = \frac{1}{2}\left[\left(\mathbf{q}_{Ti}^{n} + \mathbf{q}_{Ti}^{n*}\right) + \mathbf{K}\left(\mathbf{q}_{T_i}^{n*}\right)\right], \tag{7}$$

where

$$\mathbf{q}_{T_i}^{n*} = \mathbf{q}_{T_i}^{n} + \mathbf{K}\left(\mathbf{q}_{T_i}^{n}\right), \tag{8}$$

and $\mathbf{K}(\mathbf{q}_{T_i}^{n})$ is given by

$$\mathbf{K}\left(\mathbf{q}_{T_i}^{n}\right) = \frac{\Delta t^n}{\Omega}\left[\int_{\Omega} \mathbf{S}(\mathbf{q}^n)\mathrm{d}\Omega - \sum_{k=1}^{3} \mathbf{F}_k(\mathbf{q}^n)\cdot\mathbf{n}_k l_k\right]. \tag{9}$$

Since the explicit scheme is used, the Courant–Friedrichs–Lewy (CFL) condition must be satisfied to ensure solution stability. In this work, the CFL condition as proposed in Delis et al. (2011) and Delis and Nikolos (2013) is employed to estimate the time step on triangular grids:

$$\Delta t = \mathrm{CFL}\min\left(\frac{R_{T_i}}{\sqrt{u_{T_i}^2 + v_{T_i}^2} + \sqrt{gh_{T_i}}}\right), \tag{10}$$

where R_{T_i} is the minimum distance from the centroid to the edges of the ith triangle, CFL denotes the Courant number and CFL = 0.5 is adopted in this work for all of the simulations.

3.3. Novel MUSCL scheme to evaluate the values of flow variables at the midpoints of cell edges

To compute the fluxes and the slope source terms, the values of the flow variables at the midpoints of the cell edges are required. However, as mentioned in the Introduction, the existing techniques to compute these values are relatively complicated on unstructured grids. For example, the technique in Hou et al. (2013a) extrapolates the values at D and then extrapolates them again from D to M. In this regard, a straightforward MUSCL scheme is highly desired to extrapolate the required values directly to the edge midpoints. This work devises such a MUSCL scheme which is incorporated into a 2D cell-centered Godunov-type finite volume model as proposed in Hou et al. (2013a,c) to solve the SWEs on unstructured grids. Using

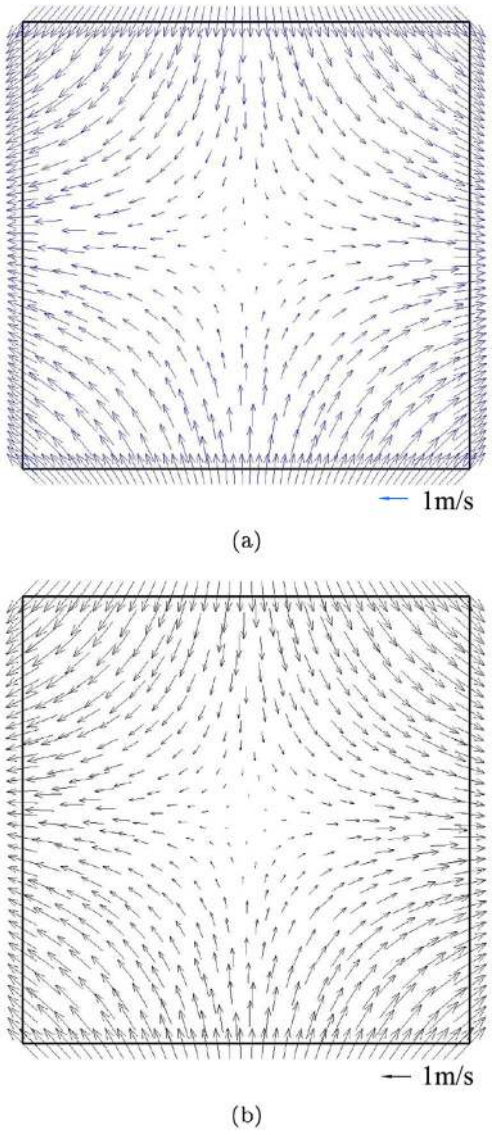

Fig. 9. Steady flow over uneven bed: flow field on the Delaunay grid: (a) exact solution; (b) computed result by the new MUSCL scheme.

Table 1
Steady flow over uneven bed: *RRMSE* at $t = 25$ s and relative computational cost on different grids.

Schemes	Grids	*RRMSE* (h)[%]	*RRMSE* (q_x)[%]	*RRMSE* (q_y)[%]	Relative computational time
New MUSCL scheme	Type A	0.4333	3.5311	4.0076	1.000
MUSCL scheme in Hou et al. (2013a)	Type A	0.4406	3.4813	4.4460	1.065
New MUSCL scheme	Type B	0.4209	3.5526	3.7058	1.174
MUSCL scheme in Hou et al. (2013a)	Type B	0.4230	3.7574	3.9242	1.234
New MUSCL scheme	Type C	0.4437	3.8283	3.5450	1.145
MUSCL scheme in Hou et al. (2013a)	Type C	0.4468	3.7849	3.6527	1.204
New MUSCL scheme	Type D	0.5177	4.0291	5.6376	1.108
MUSCL scheme in Hou et al. (2013a)	Type D	0.5246	4.1230	5.5567	1.179

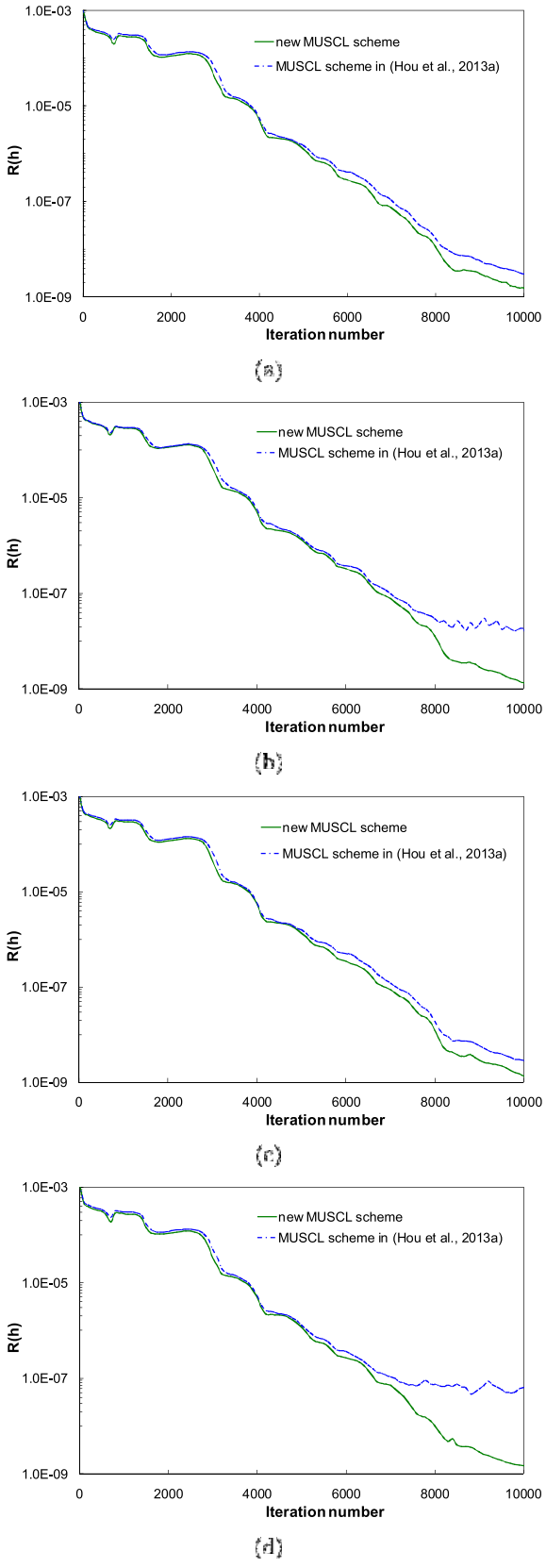

Fig. 10. Steady flow over frictional uneven bed: relative root mean square errors for h on different grids: (a) type A, (b) type B, (c) type C, (d) type D.

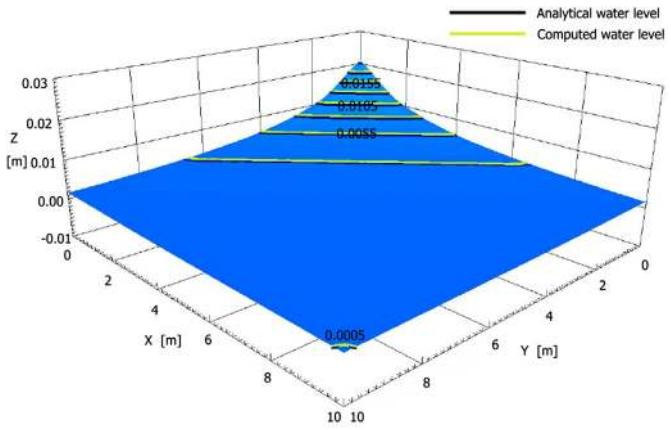

Fig. 11. Steady flow over frictional uneven bed: exact water level contours and those computed by the new MUSCL scheme on the Delaunay grid [m].

the MUSCL scheme as proposed herein, the required values can be sought in two steps: 1) values at the cell nodes are evaluated; and 2) these nodal values are used to construct the slopes which are then limited to extrapolate the values at midpoints of the cell edges.

3.3.1. Evaluating nodal values

In a cell-centered finite volume method, since the flow information is stored at the cell centroids, the nodal values can be evaluated from those at the centroids of the surrounding cells using the weighted average method. Based on inverse distance interpolation (Frink, 1991; Park et al., 2010), the values at the ith node N_i are calculated by

$$\mathbf{q}_{N_i} = \frac{\sum_{k=1}^{n_c} \left(\mathbf{q}_{T_i} / |\mathbf{r}_{N_i,T_k}|\right)}{\sum_{k=1}^{n_c} \left(1/|\mathbf{r}_{N_i,T_k}|\right)}, \tag{11}$$

where $\mathbf{q}_{N_i}$ contains the nodal values at node N_i, $\mathbf{q}_{T_i}$ consists of the values at the centroid of cell T_i, $\mathbf{r}_{N_i,\,T_k}$ denotes the distance between the centroid of the kth neighboring cell and node N_i (see Fig. 2), n_c is the total number of neighboring cells of node N_i.

3.3.2. Constructing slopes

To implement the MUSCL scheme, two sets of slopes are introduced. They are respectively defined as the upstream and downstream slopes. In this subsection, the procedure to construct the slopes for the first edge E_1 of cell T_i is demonstrated and those for other edges can be sought in a similar way (Fig. 3). The downstream slopes are built from the values at the midpoint of the edge and those at the cell centroid.

$$(\nabla \mathbf{q})_L^{\text{down}} = \frac{\overline{\mathbf{q}}_M^L - \mathbf{q}_{T_i}}{|\mathbf{r}_{T_1,M}|}, \tag{12}$$

where $\overline{\mathbf{q}}_M^L$ contains the unlimited values at the left hand side of E_1 and is computed by the available values of the two adjacent nodes at this edge as

$$\overline{\mathbf{q}}_M^L = \frac{\mathbf{q}_{N_2} + \mathbf{q}_{N_3}}{2}, \tag{13}$$

In triangular cells, since the line connecting the cell centroid and the midpoint E_1 also passes through node N_1, the upstream slopes for this edge can be easily constructed from the values at the cell centroid and those at node N_1 that is opposite to E_1

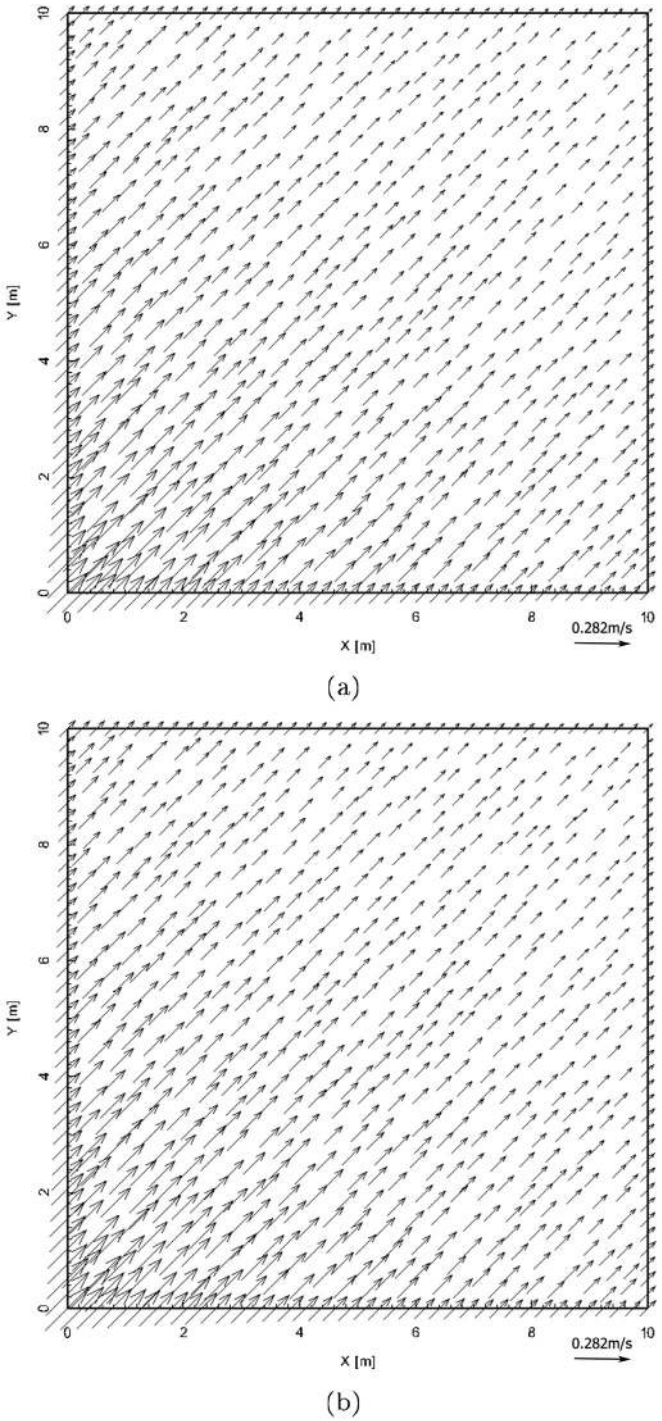

Fig. 12. Steady flow over frictional uneven bed: flow field of: (a) exact solution; (b) computed result by the new MUSCL scheme on the Delaunay grid.

$$(\nabla \mathbf{q})_L^{\text{up}} = \frac{\mathbf{q}_{T_i} - \mathbf{q}_{N_1}}{|\mathbf{r}_{N_1,T_i}|}. \tag{14}$$

3.3.3. Calculating values at the midpoint

Once the upstream and downstream slopes are available, the values at the midpoint of a cell edge can be obtained using a classical MUSCL scheme, in which the slopes are limited to give rise to oscillation-free solutions. Again taking midpoint M at edge E_1 as an example, the extrapolated values at the left hand side of M are given by

Table 2
Steady flow over frictional uneven bed: *RRMSE* at $t = 20$ s and relative computational cost on different grids.

Schemes	Grids	*RRMSE* (h)[%]	*RRMSE* (q_x)[%]	*RRMSE* (q_y)[%]	Relative computational time
New MUSCL scheme	Type A	0.0538	0.6023	0.6664	1.000
MUSCL scheme in Hou et al. (2013a)	Type A	0.0871	0.6531	0.6558	1.071
New MUSCL scheme	Type B	0.0372	0.3461	0.3237	1.102
MUSCL scheme in Hou et al. (2013a)	Type B	0.0837	0.4124	0.4345	1.181
New MUSCL scheme	Type C	0.0503	0.6127	0.6881	1.022
MUSCL scheme in Hou et al. (2013a)	Type C	0.0838	0.6335	0.6824	1.064
New MUSCL scheme	Type D	0.0577	0.4739	0.4265	1.113
MUSCL scheme in Hou et al. (2013a)	Type D	0.1054	0.5362	0.4753	1.169

$$\mathbf{q}_M^L = \mathbf{q}_{T_i} + \mathbf{r}_{T_i,M}\psi\left[(\nabla\mathbf{q})_L^{\text{down}}, (\nabla\mathbf{q})_L^{\text{up}}\right], \tag{15}$$

where $\psi(a, b)$ is the limiting function with two arguments a and b. Van Albada limiter (van Albada et al., 1982) is chosen in this work due to its advantages in maintaining higher-order accuracy for smooth solution and ensuring convergence to steady-state, which may be expressed as

$$\psi(a,b) = \begin{cases} \dfrac{(a^2+e)b + (b^2+e)a}{a^2+b^2+2e}, & \text{if } ab > 0, \\ 0, & \text{if } ab \le 0, \end{cases} \tag{16}$$

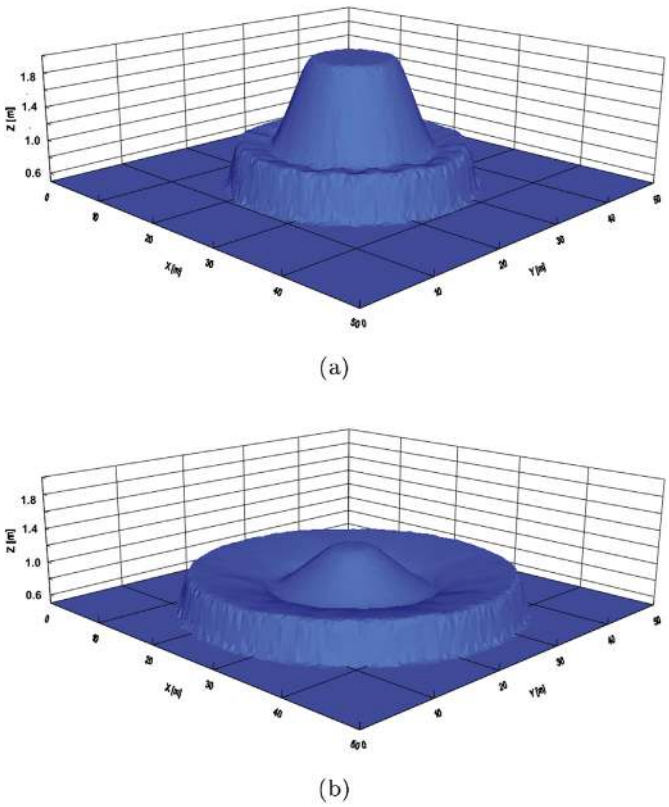

Fig. 13. Circular dam-break problem: 3D view of water level computed by the new MUSCL scheme at: (a) $t = 1.0$ s, (b) $t = 2.5$ s.

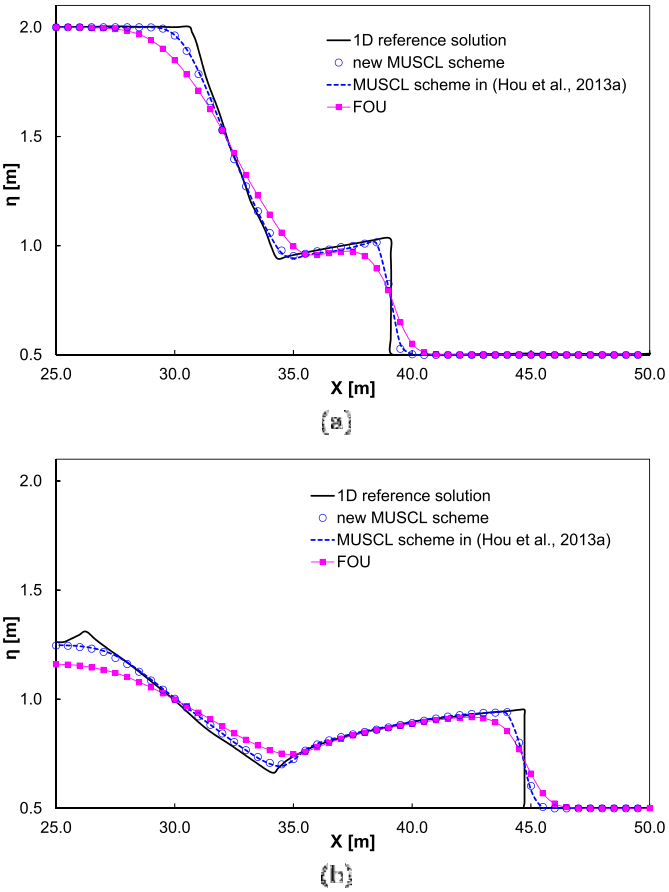

Fig. 14. Circular dam-break problem: sectional view of the computed water level on the Delaunay grid at: (a) $t = 1.0$ s, (b) $t = 2.5$ s.

where e is introduced to prevent division by zero and $e = 10^{-16}$ is adopted (Nikolos and Delis, 2009; Delis et al., 2011; Delis and Nikolos, 2013; Hou et al., 2013a). Using the same approach, the values at the right hand side of M can be obtained by,

$$\mathbf{q}_M^R = \mathbf{q}_{T_j} + \mathbf{r}_{T_j,M}\psi\left[(\nabla\mathbf{q})_R^{\text{down}}, (\nabla\mathbf{q})_R^{\text{up}}\right], \tag{17}$$

in which $\mathbf{q}_{T_j}$ represents the values at the centroid of cell T_j, $(\nabla\mathbf{q})_R^{\text{down}}$ and $(\nabla\mathbf{q})_R^{\text{up}}$ can be calculated using Equations (12) and (14) and the nodal values of cell T_j.

Table 3
Circular dam break: *RRMSE* and relative computational cost on different grids.

Schemes	Grids	*RRMSE*(h) at $t = 1.0$ s [%]	*RRMSE*(h) at $t = 2.5$ s [%]	Relative computational time
New MUSCL scheme	Type A	4.2094	2.9985	1.000
MUSCL scheme in Hou et al. (2013a)	Type A	4.2123	3.0028	1.058
New MUSCL scheme	Type B	3.6655	2.0092	1.115
MUSCL scheme in Hou et al. (2013a)	Type B	3.6697	2.0124	1.185
New MUSCL scheme	Type C	3.7937	1.9512	1.107
MUSCL scheme in Hou et al. (2013a)	Type C	3.7954	1.9556	1.179
New MUSCL scheme	Type D	4.6435	2.4540	1.241
MUSCL scheme in Hou et al. (2013a)	Type D	4.6493	2.4606	1.294

Note: the 1D reference solution is used as $\bar{\mathbf{q}}_{T_i}$ in Equation (34) to compute *RRMSE*(h).

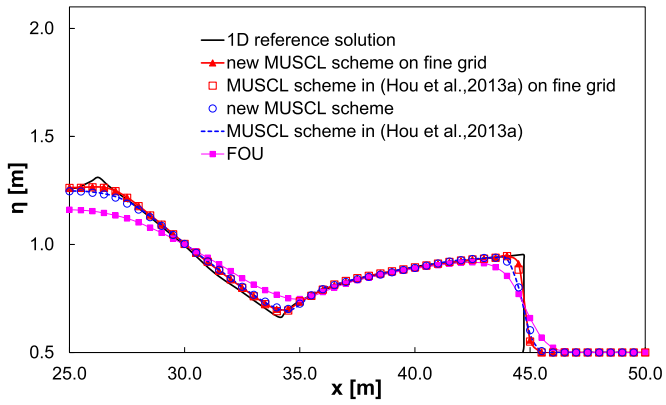

Fig. 15. Circular dam-break problem: sectional view of the computed water level on the Delaunay grid at $t = 2.5$ s.

Whist the new MUSCL scheme is developed on the basis of the 1D MUSCL scheme which is surely capable of preserving monotonicity for 1D problems, it is not easy to prove that the extrapolated values at the edge midpoints are not local extrema in multi-dimensional problems, due to the complex geometry and topology. The appearance of local extrema is generally recognized as violating the monotonicity. Liu (1993) proposed a local maximum principle to avoid overshoot and undershoot when constructing slopes for multi-dimensional problems. That is, the extrapolated values at edge midpoints or cell nodes must not be higher than the local maximum values and lower than the local minimum values, for example in Hubbard (1999) and Park et al. (2010). According to this idea, the extrapolated values by the new MUSCL scheme are constrained by,

$$\begin{aligned} &\min\left(\mathbf{q}_{T_i},\mathbf{q}_{T_j},\mathbf{q}_{N_2},\mathbf{q}_{N_3}\right)\leqslant \mathbf{q}_M^L \leqslant \max\left(\mathbf{q}_{T_i},\mathbf{q}_{T_j},\mathbf{q}_{N_2},\mathbf{q}_{N_3}\right),\\ &\min\left(\mathbf{q}_{T_i},\mathbf{q}_{T_j},\mathbf{q}_{N_2},\mathbf{q}_{N_3}\right)\leqslant \mathbf{q}_M^R \leqslant \max\left(\mathbf{q}_{T_i},\mathbf{q}_{T_j},\mathbf{q}_{N_2},\mathbf{q}_{N_3}\right), \end{aligned} \tag{18}$$

where $\mathbf{q}_{T_i},\mathbf{q}_{T_j},\mathbf{q}_{N_2},\mathbf{q}_{N_3}$ are the values at the cell centers and the nodes adjacent to the midpoint under consideration, see Fig. 1. As $\mathbf{q}_{N_2}$ and $\mathbf{q}_{N_3}$ are obtained from inverse distance interpolation, they are absolutely not new local extrema. Using this constraint, the possible new local extrema caused by Equations (15) and (17) are completely avoided in a simple way.

Comparing with the prevailing 2D edge-based MUSCL schemes, for example in Delis et al. (2011), Buffard and Clain (2010), Delis and Nikolos (2013) and Hou et al. (2013a), the current MUSCL scheme provides a direct and simple way for calculating the required values at the midpoints of the cell edges. To be more specific, the new scheme demands less storage since it involves directly nodal values while other schemes commonly use the gradients at cells; the number of nodes is typically much less than the number of cells (1/2 in general). Moreover, the new scheme takes the advantage of the geometry of the triangular cells, i.e. slopes are constructed along the line passing through the midpoint of the edge under consideration, the cell centroid and a node where the values are easy to obtain or already available. This therefore represents a more efficient scheme. In addition, the new scheme is straightforward to extend to solve 3D problems by utilising tetrahedron grids. In a tetrahedron cell, the required values at face centers can be extrapolated from the cell center in a similar way, using nodal values computed from Equation (11) to construct the upstream and downstream slopes. Obviously, the current MUSCL scheme is developed in a general way and thus is not restricted to solve only the SWEs. It can also be applied to solve other hyperbolic equations

Table 4
2D Riemann problem: initial flow conditions.

Region	Coordinates [m]	h [m]	u [ms^{-1}]	v [ms^{-1}]
1	$x \leq 100, y \leq 100$	1.0	10.0	10.0
2	$x > 100, y \leq 100$	1.0	0.0	10.0
3	$x \leq 100, y > 100$	1.0	10.0	0.0
4	$x > 100, y > 100$	10.0	0.0	0.0

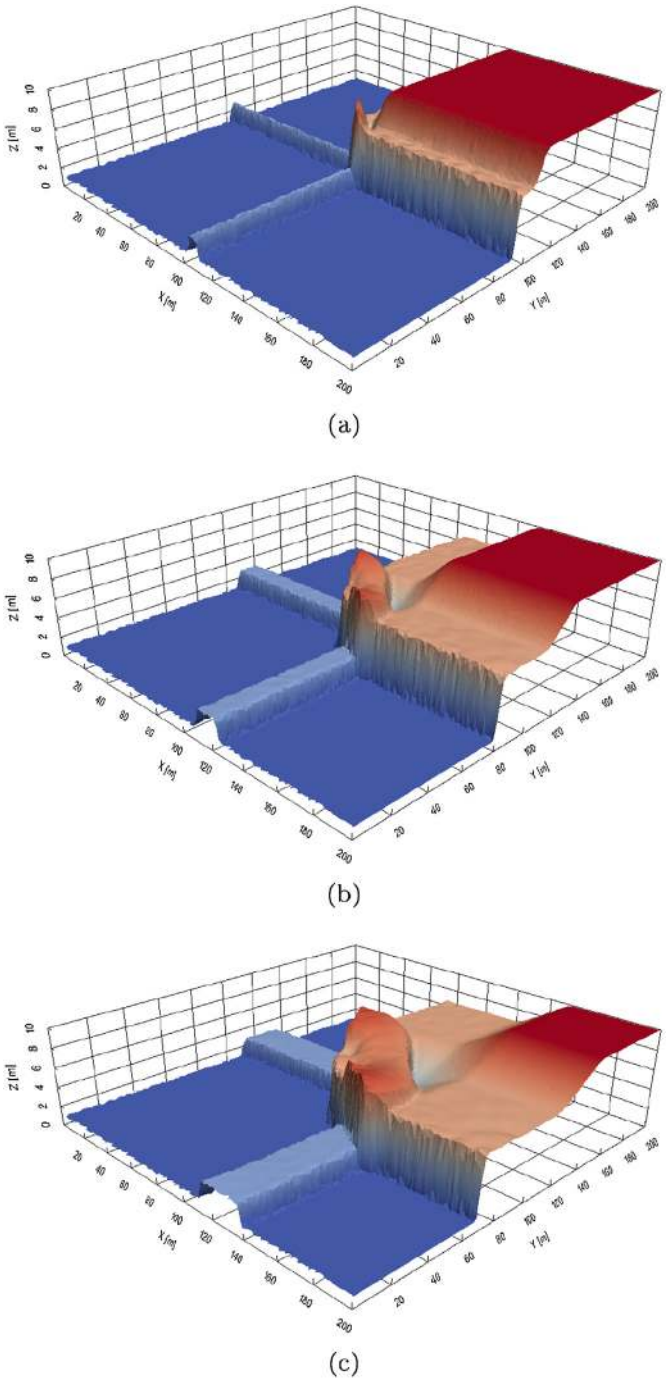

Fig. 16. 2D Riemann problem: computed flow patterns in 3D view by the new MUSCL scheme on Delaunay grid at: (a) $t = 1$ s, (a) $t = 3$ s and (c) $t = 5$ s.

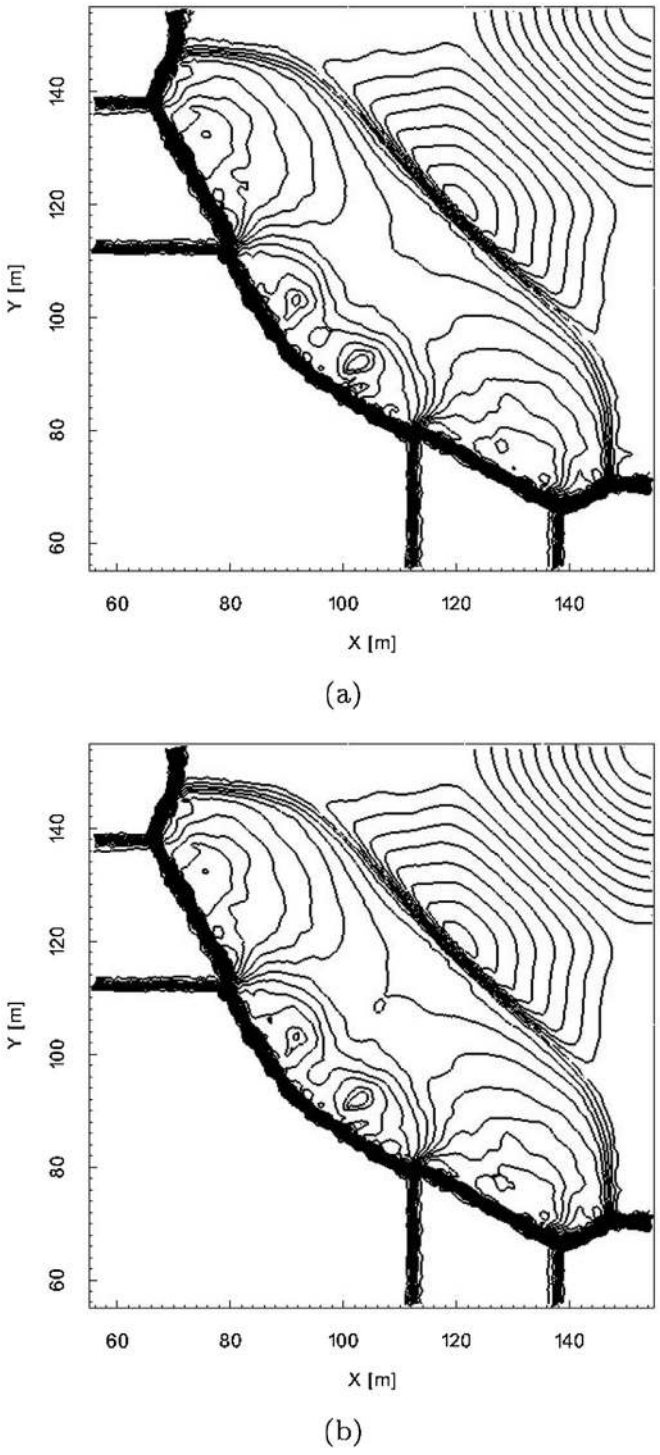

Fig. 17. 2D Riemann problem: computed vectors of unit-width discharge and contours of water depth on the Delaunay grid at $t = 5$ s by: (a) the MUSCL scheme in Hou et al. (2013a), (b) the new MUSCL scheme. Equidistance of Contour lines 0.25 m.

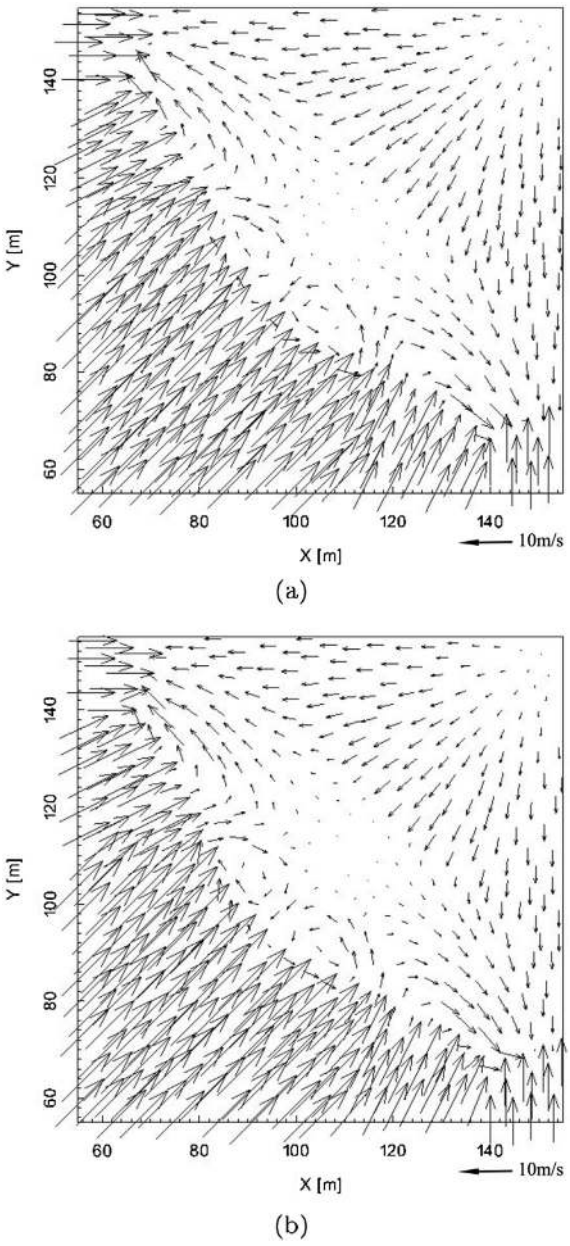

Fig. 18. 2D Riemann problem: computed velocities on the Delaunay grid at $t = 5$ s by: (a) the MUSCL scheme in Hou et al. (2013a), (b) the new MUSCL scheme.

that are widely used in environmental modeling, e.g. the advection–diffusion equations (Rubio et al., 2008; Ani et al., 2009; Gomez and Tchijov, 2010; Liang et al., 2010; Kong et al., 2013; Kourakos and Harter, 2014).

3.3.4. Midpoint values of flow variables for SWEs

To preserve the C-property, only η, h, q_x and q_y are extrapolated by Equations (15) and (17) to the midpoint of interest to give η_M^L, η_M^R, h_M^L, h_M^R, q_{xM}^L, q_{xM}^R, q_{yM}^L and q_{yM}^R, respectively, following Audusse et al., 2004, Audusse and Bristeau, 2005, Liang and Borthwick, 2009, Liang and Marche, 2009, Liang, 2010, Wang et al., 2011 and Hou et al., 2013a,c. The bed elevations z_{bM}^L and z_{bM}^R are redefined as

$$z_{bM}^L = \eta_M^L - h_M^L, \quad z_{bM}^R = \eta_M^R - h_M^R. \tag{19}$$

Accordingly, the corresponding velocities at M can be calculated by,

$$u_M^L = q_{xM}^L \big/ h_M^L, \quad v_M^L = q_{yM}^L \big/ h_M^L, \quad u_M^R = q_{xM}^R \big/ h_M^R, \quad v_M^R = q_{yM}^R \big/ h_M^R. \tag{20}$$

The above $\mathbf{q}_M^L$ and $\mathbf{q}_M^R$ are then employed to evaluate the fluxes and the slope source terms in the following subsections. It should be noted that spurious velocities with local extreme values is likely

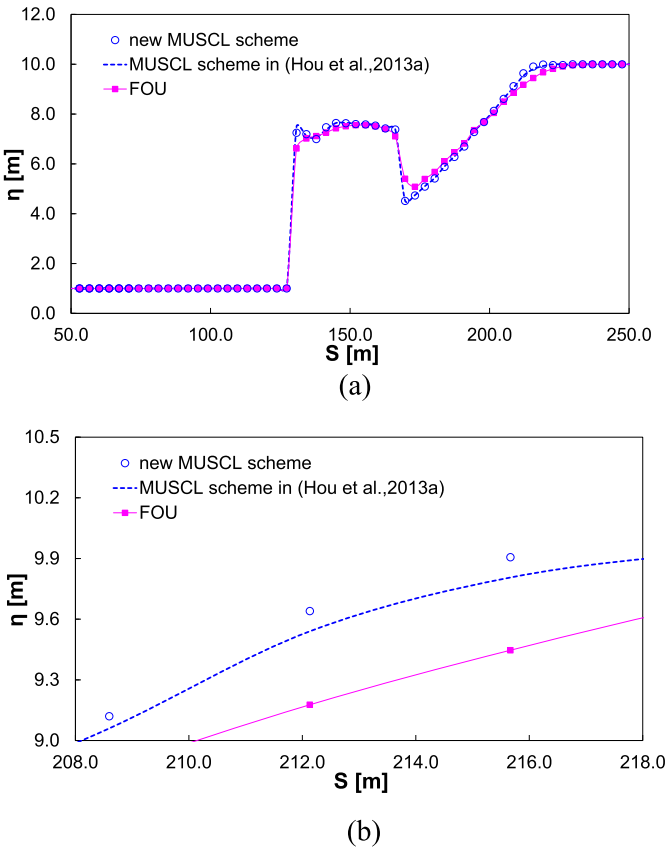

Fig. 19. 2D Riemann problem: computed water level on the Delaunay grid: (a) across the diagonal section at $t = 5$ s, (b) local zoomed-in view of (a).

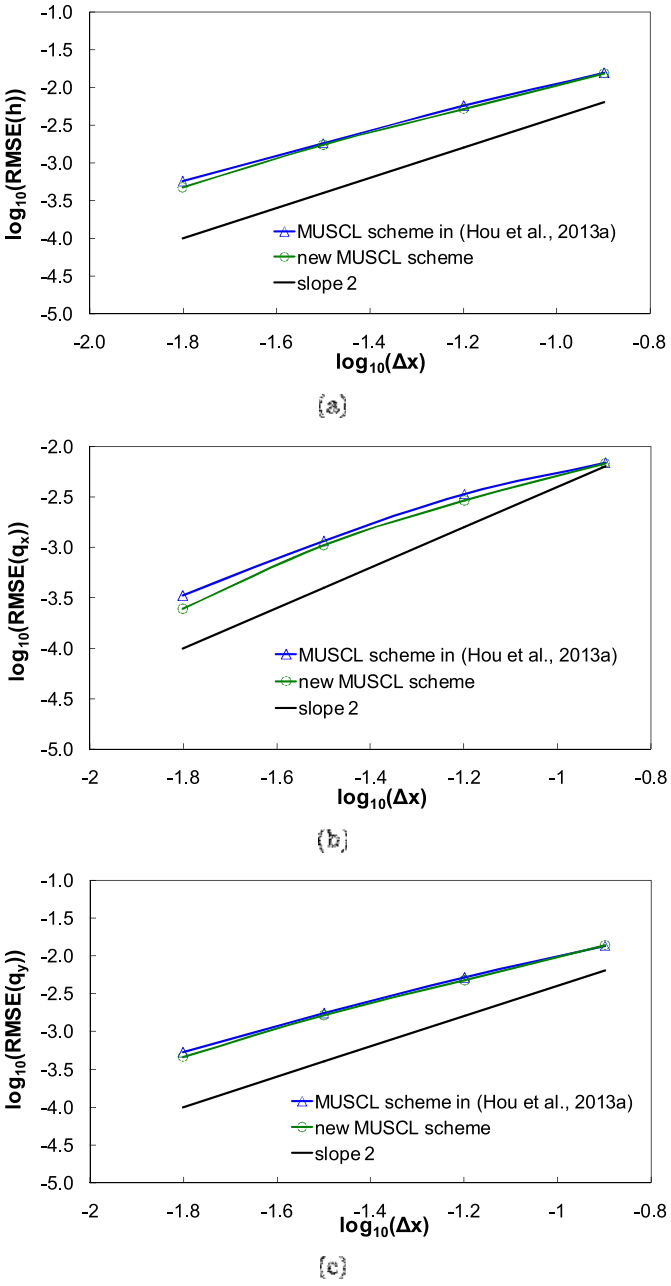

Fig. 20. Thacker's planar solution: grid convergence of the present model in terms of *RMSE* on Delaunay grids at $t = 4$T: (a) h, (b) q_x, (c) q_y.

to be calculated with the MUSCL scheme when using the conserved flow variables for a case involves rapidly changing small water depth over rough terrains (Hou et al., 2013b). Those problematic cells are normally located near the wet-dry fronts. In order to prevent the potential numerical instabilities, the MUSCL scheme is disabled at these cells and first-order scheme is used instead. That is, the values at the midpoint of the edges are assumed the same as those at the cell centroid. The problematic cells are identified according to the criteria as presented in Hou et al. (2013b). In addition, first-order scheme is also imposed at those dry cells that are adjacent to a wet cell. Other dry cells away from the wet-dry front are not taken into account during the computation. As a summary, the second-order MUSCL scheme is switched to first-order locally in a cell satisfying the following conditions

$$h_M^L \leqslant \min\left(\left|z_{bM}^L - z_{bT_i}\right|, 0.25h_{T_i}\right) \quad \text{or} \quad h_{T_i} \leqslant \varepsilon_{wd}, \tag{21}$$

where h_M^L and z_{bM}^L are the values of the flow variables computed by the MUSCL scheme and ε_{wd} is the depth tolerance used to distinguish wet and dry cells and $\varepsilon_{wd} = 1 \times 10^{-6}$ m is generally adopted (Brufau et al., 2004; Begnudelli and Sanders, 2006, 2007; Zokagoa and Soulaimani, 2010; Hou et al., 2013a,c).

3.4. Non-negative depth reconstruction

To preserve non-negative water depth and C-property, the non-negative water depth reconstruction as proposed by Audusse et al. (2004) is adopted in this work. Using this reconstruction, the water depths at the midpoint of the edge under consideration are reconstructed by,

$$h_M^L = \max\left(0, \eta_M^L - z_{bM}\right), \quad h_M^R = \max\left(0, \eta_M^R - z_{bM}\right), \tag{22}$$

where

$$z_{bM} = \max\left(z_{bM}^L, z_{bM}^R\right). \tag{23}$$

Accordingly, the unit-width discharges at M are recomputed by the reconstructed water depths in Equation (22).

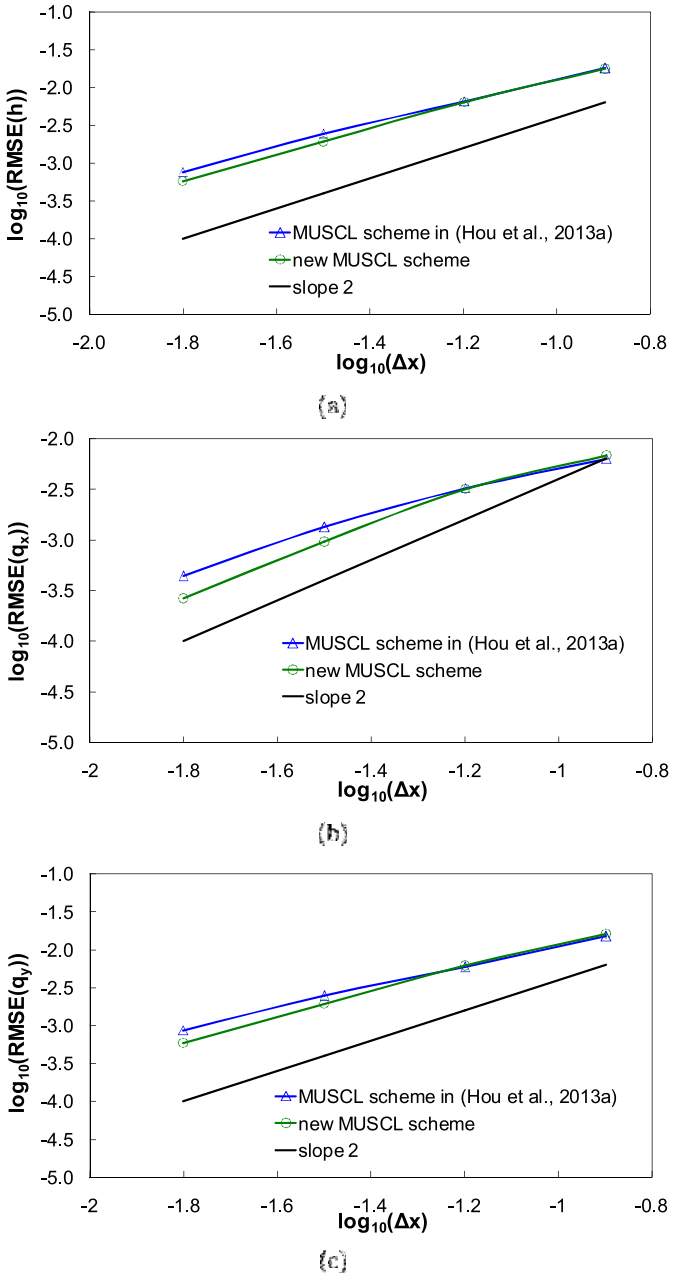

Fig. 21. Thacker's planar solution: grid convergence of the present model in terms of *RMSE* on Scottish grids at $t = 4$T: (a) h, (b) q_x, (c) q_y.

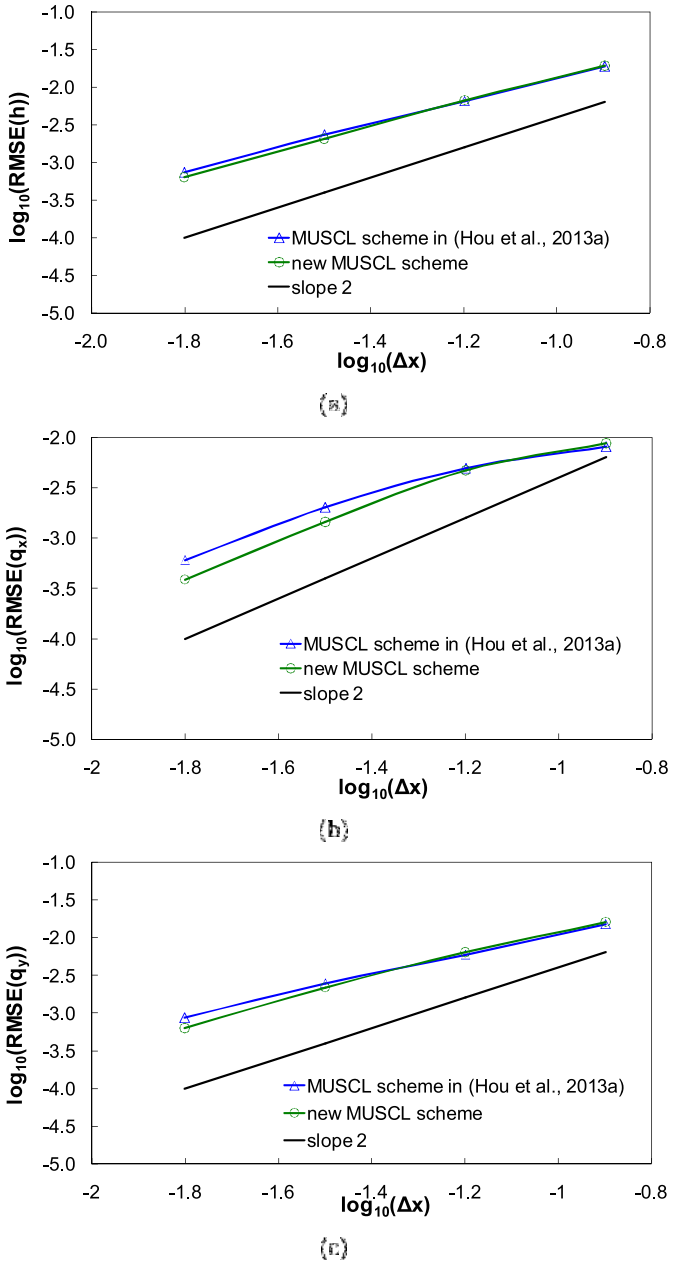

Fig. 22. Thacker's planar solution: grid convergence of the present model in terms of *RMSE* on diagonal grids at $t = 4$T: (a) h, (b) q_x, (c) q_y.

$$q_{xM}^L = h_M^L u_M^L,\quad q_{yM}^L = h_M^L v_M^L,\quad q_{xM}^R = h_M^R u_M^R,\quad q_{yM}^R = h_M^R v_M^R, \tag{24}$$

where u_M^L, v_M^L, u_M^R and v_M^R are evaluated from Equation (20). These reconstructed edge values of the flow variables are then employed to compute the interface fluxes and the slope source terms.

3.5. Calculating fluxes and source terms

The HLLC approximate Riemann solver developed by Toro et al. (1994) is applied in this work to compute the interface fluxes ($\mathbf{F}_k(\mathbf{q})\cdot\mathbf{n}_k$ in Equation (6)), which can be directly apply to shallow water flows with shocks and wet-dry interfaces (Liang and Marche, 2009; Liang and Borthwick, 2009; Liang, 2010; Song et al., 2011b,a; Wang et al., 2011; Hou et al., 2013a,c,b). The detailed implementation of the HLLC approximate Riemann solver on unstructured grids can be found in (Song et al., 2011a; Hou et al., 2013c).

The slope flux method presented in (Hou et al., 2013c), suitable for unstructured grids, is adopted to evaluate the slope source terms $\mathbf{S}_b$. The slope source terms in the cell under consideration (the left cell in this work) are transformed into fluxes through the edges of this cell, i.e.,

$$\begin{aligned}\oint_\Omega \mathbf{S}_b \mathrm{d}\Omega &= \oint_\Gamma \mathbf{F}_{Sk}(\mathbf{q})\mathrm{d}\Gamma,\\ &= \sum_{k=1}^{3}[\mathbf{F}_{Sk}(\mathbf{q})l_k].\end{aligned} \tag{25}$$

The slope flux vector $\mathbf{F}_{Sk}(\mathbf{q}^n)$ at the midpoint of the edge being considered is given by,

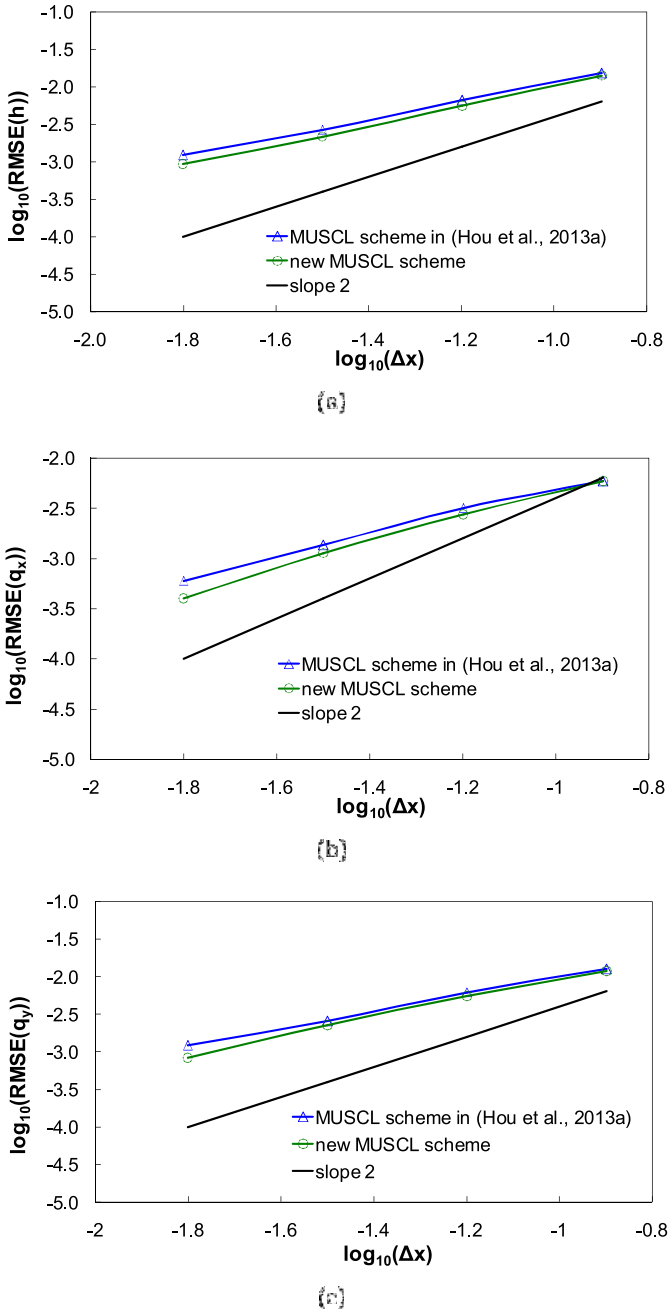

Fig. 23. Thacker's planar solution: grid convergence of the present model in terms of *RMSE* on distorted grids at $t = 4T$: (a) h, (b) q_x, (c) q_y.

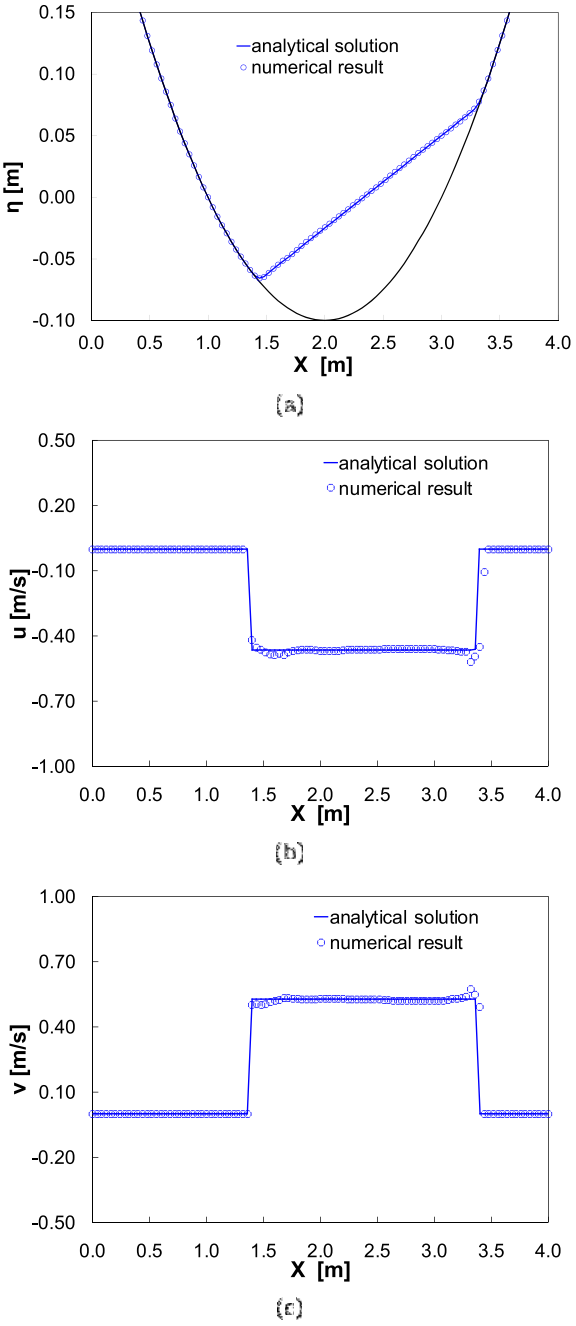

Fig. 24. Thacker's planar solution: computed results using the new MUSCL scheme at $t = 2.11T$: (a) η, (b) u, (c) v.

$$\mathbf{F}_{SM}(\mathbf{q}) = \begin{bmatrix} 0 \\ -n_{Mx} g\left(h_M^L + h_{T_i}\right)\left(z_{bM} - z_{bT_i}\right)/2 \\ -n_{My} g\left(h_M^L + h_{T_i}\right)\left(z_{bM} - z_{bT_i}\right)/2 \end{bmatrix}, \tag{26}$$

in which the modified bed elevation at the edge is used and,

$$z_{bM} \leftarrow \min\left(z_{bM}, \eta_M^L\right), \tag{27}$$

and $(n_{Mx}, n_{My})^T$ is the outward normal vector of the edge of interest.

With respect to the friction source terms, a prevalent method known as splitting point-implicit method proposed in Bussing and Murmant (1988) is adopted. Moreover, in order to prevent the reverse flow direction caused by unrealistic friction, a limiting step introduced by Liang and Marche (2009) is taken into account. The more complete description of this method for 2D schemes can be found in Hou et al. (2013c, b).

3.6. Boundary conditions

The theory of characteristics is considered to be adequate to estimate the unknown variables at boundaries when solving the SWEs. Based on the flow variables at the boundaries, the interface fluxes through cell edges defining the physical boundaries can be directly computed. In this work, the detailed boundary treatment is demonstrated at a boundary edge e as shown in Fig. 4. At first, the

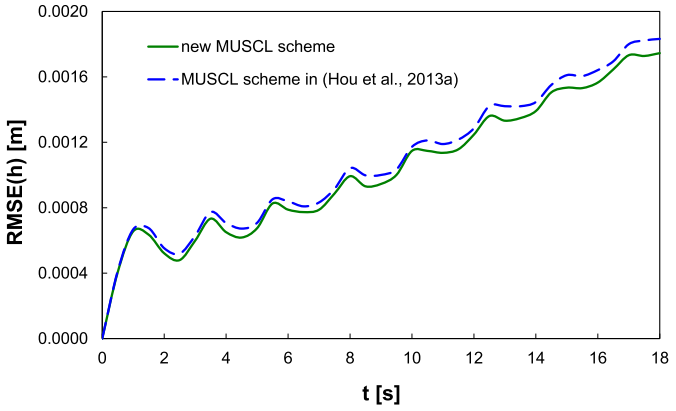

Fig. 25. Thacker's planar solution: *RMSE* history of the computed water depth on the Delaunay grid.

values of flow variables on the inner side of the midpoint M are computed from those at the two adjacent nodes N_2 and N_3 as,

$$\mathbf{q}_M^L = \frac{\mathbf{q}_{N_2} + \mathbf{q}_{N_3}}{2}, \tag{28}$$

where the nodal values $\mathbf{q}_{N_2}$ and $\mathbf{q}_{N_3}$ are obtained from Equation (11) by using the inverse distance interpolation. The bed elevations on the left and right sides of a boundary are assumed to be the same. Therefore, z_{bM} (equation (23)) used in the computation of flux and slope source terms is equal to z_{bM}^L. Next, the fluxes through the boundaries are calculated as in Hou et al. (2013c). For open and solid boundaries, the fluxes are computed respectively by the Riemann solver and directly by Equation (5).

3.6.1. Open boundary conditions

At open boundary, the fluxes are evaluated by the Riemann solver. Since the inner values $\mathbf{q}_M^L$ are available, the outer values of flow variables $\mathbf{q}_M^R$ are required by the Riemann solver. As in Hou et al. (2013c), $\mathbf{q}_M^R$ are calculated in different ways according to different flow conditions as listed below.

3.6.1.1. Subcritical flow. When h_M^R is given, the velocity normal to the boundary $u_M^{\perp R}$ can be computed from the theory of characteristics as

$$u_M^{\perp R} = u_M^{\perp L} + 2\sqrt{gh_M^L} - 2\sqrt{gh_M^R}. \tag{29}$$

If $u_M^{\perp R}$ is specified, the unknown h_M^R can be evaluated by,

$$h_M^R = \frac{\left(u_M^{\perp L} + 2\sqrt{gh_M^L} - u_M^{\perp R}\right)^2}{4g}, \tag{30}$$

In the case of a given $q_M^{\perp R}$, h_M^R and $u_M^{\perp R}$ can be computed from the relationship of $q_M^{\perp R} = h_M^R u_M^{\perp R}$ and the theory of characteristics, by means of Newton–Raphson iterative method.

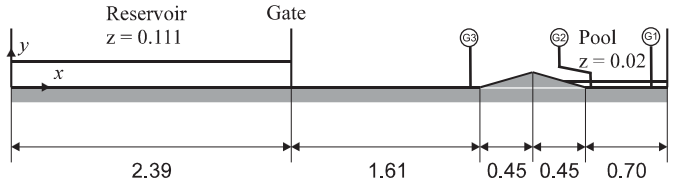

Fig. 26. Dam-break over a bump: experimental setup and initial conditions (Soares-Frazão, 2007) [m].

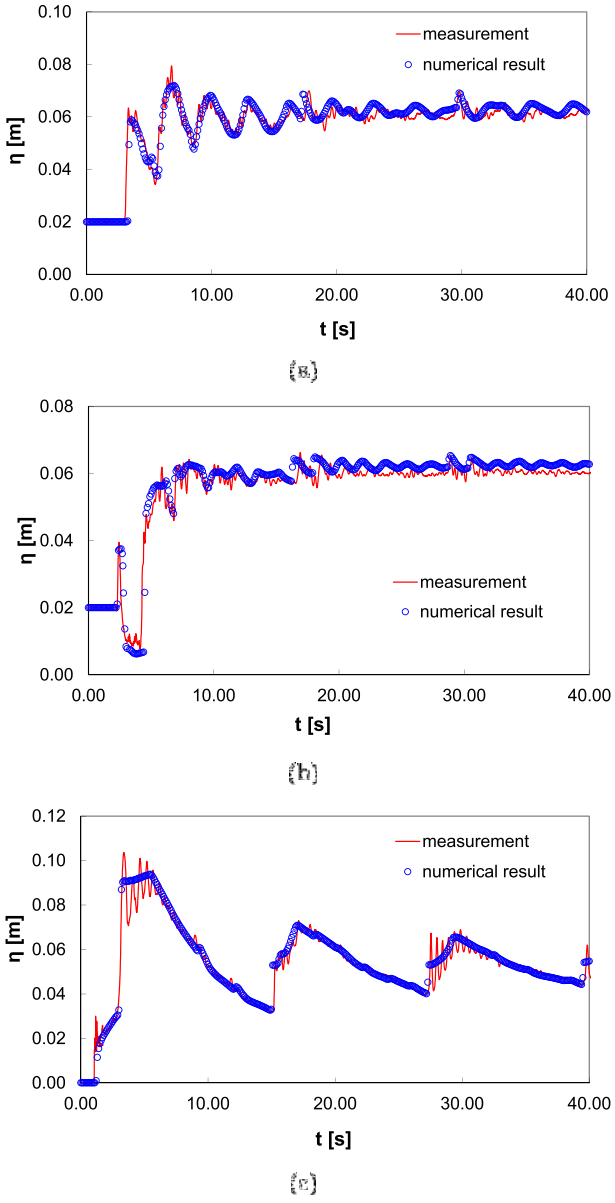

Fig. 27. Dam-break over a bump: water level changes with time at: (a) gauge 1, (b) gauge 2, (c) gauge 3.

Once h_M^R and $u_M^{\perp R}$ are obtained, u_M^R and v_M^R can be calculated by

$$\begin{aligned} u_M^R &= u_M^{\perp R} n_x - u_M^{\parallel R} n_y, \\ v_M^R &= u_M^{\parallel R} n_x + u_M^{\perp R} n_y, \end{aligned} \tag{31}$$

where $u_M^{\parallel R}$ is the tangential velocity to the boundary and is assumed to be the same as $u_M^{\parallel L}$ (Song et al., 2011a). Finally, we obtain $q_{xM}^R = h_M^R u_M^R$ and $q_{yM}^R = h_M^R v_M^R$.

3.6.1.2. Supercritical flow. For a supercritical flow, h_M^R, q_{xM}^R and q_{yM}^R either need to be prescribed at the inflow boundary or are equal to h_M^L, q_{xM}^L and q_{yM}^L at the outflow boundary.

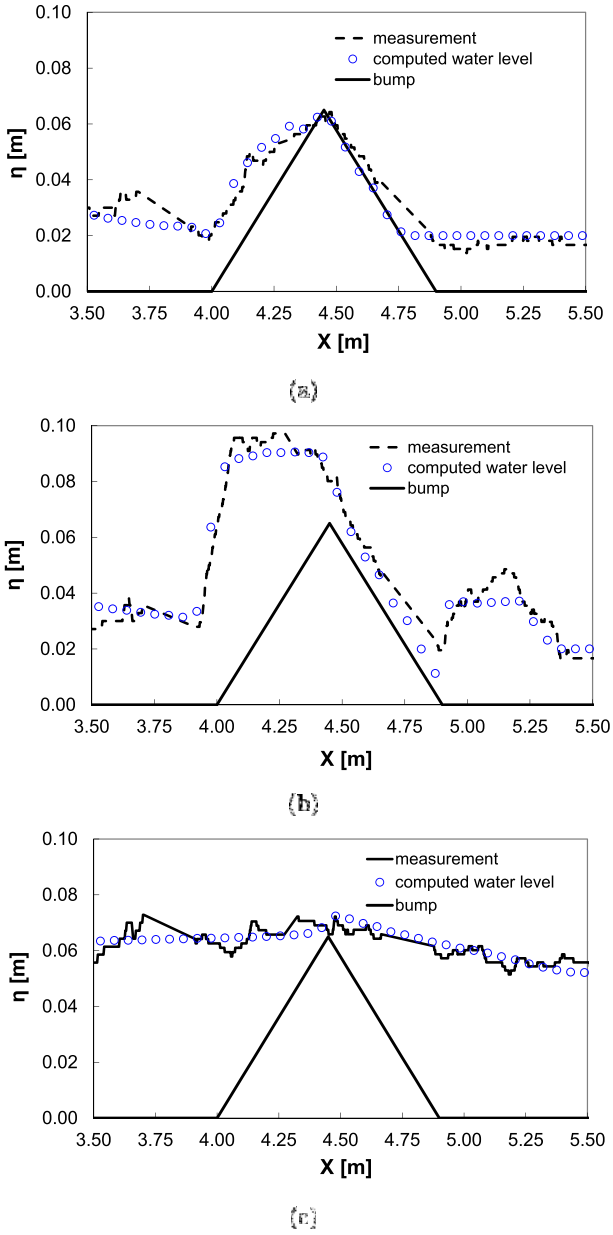

Fig. 28. Dam-break over a bump: computed and measured water levels near the bump at: (a) $t = 1.8$ s, (b) $t = 3.0$ s, (c) $t = 8.4$ s.

3.6.2. Solid boundary conditions

As in Kuiry et al. (2008), Liang and Borthwick (2009), Song et al. (2011a) and Hou et al. (2013c), the normal flux at a solid boundary is computed by,

$$\mathbf{F}(\mathbf{q})\cdot\mathbf{n} = \begin{bmatrix} 0 \\ g\left(h_M^R\right)^2 n_x \big/ 2 \\ g\left(h_M^R\right)^2 n_y \big/ 2 \end{bmatrix}, \tag{32}$$

where $h_M^R = h_M^L$.

4. Test cases

In this section, seven test cases are simulated to evaluate the performance of the novel MUSCL scheme that has been

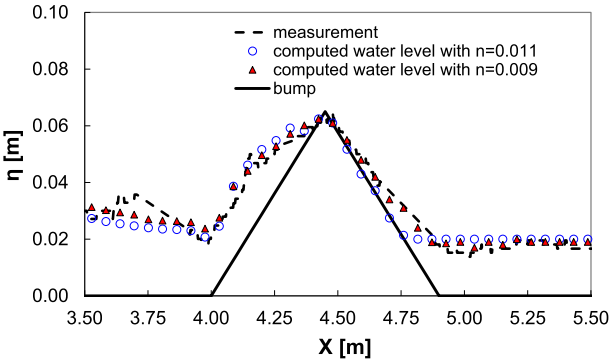

Fig. 29. Dam-break over a bump: computed water levels near the bump at $t = 1.8$ s using different Manning coefficient.

incorporated into a 2D shallow flow model, roughly following a general evaluation procedure as suggested by Bennett et al. (2013). The first step is to have a clear idea of the aim and scale of the new scheme. The aim is essentially to improve the performance of the shallow water flow model in converging to the general steady state, capturing shocks, maintaining higher-order solution accuracy and handling complex flows with wet-dry fronts over uneven beds on triangular grids. With regard to the scale, the model is valid for the shallow water problems in a wide range of scales, as long as they satisfy the long wave assumption (Hinkelmann, 2005). The second step of the performance evaluation is to check the data. The test cases selected in this work have sufficient data to carry out the performance evaluation. Since the model is physically based, the only empirical parameter as required is the Manning coefficient which is either given or assumed according to the bed materials; no calibration is necessary for all of the test cases as considered in this work. The next two steps are to assess the model performance through visual analysis that applies to all of the test cases and solution accuracy assessment that is only considered in those test cases with analytical solutions or measurements. In this work, the root mean square error is selected as the performance criteria to investigate the accuracy of the model. On unstructured grids, the volume weighted root mean square error (*RMSE*) (Sun and Takayama, 2003) and volume weighted relative root mean square error (*RRMSE*) are used, which are respectively formulated as,

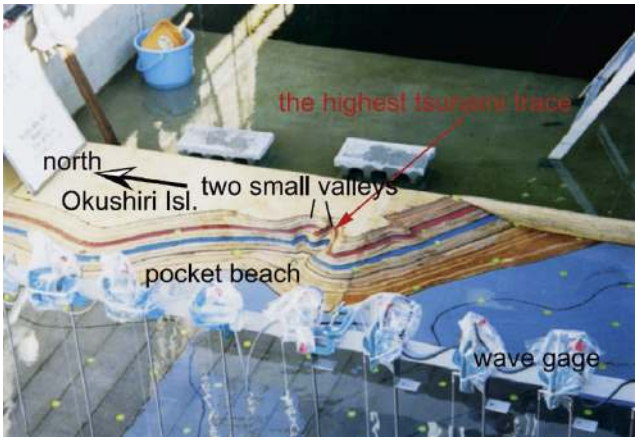

Fig. 30. Tsunami runup onto a complex beach: a photo view of the model around pocket beach in the Criepi flume (Matsuyama and Tanaka, 2001).

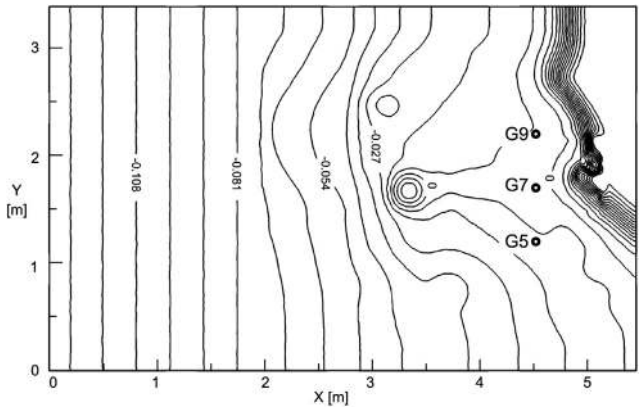

Fig. 31. Tsunami runup onto a complex beach: the domain and bathymetry for the laboratory experiment [m].

$$RMSE(\mathbf{q}) = \sqrt{\frac{\sum_{I}^{N_T}\left[\Omega_{T_i}\left(\mathbf{q}_{T_i} - \tilde{\mathbf{q}}_{T_i}\right)^2\right]}{\sum_{I}^{N_T}\Omega_{T_i}}}, \tag{33}$$

$$RRMSE(\mathbf{q}) = \sqrt{\frac{\sum_{I}^{N_T}\left[\Omega_{T_i}\left(\frac{\mathbf{q}_{T_i} - \tilde{\mathbf{q}}_{T_i}}{\tilde{\mathbf{q}}_{T_i}}\right)^2\right]}{\sum_{I}^{N_T}\Omega_{T_i}}}, \tag{34}$$

where Ω_{T_i} denotes the volume of the ith cell; N_T represents the number of cells; $\mathbf{q}_{T_i}$ and $\tilde{\mathbf{q}}_{T_i}$ are the numerical and analytical solutions or measured data at the cell centroid, respectively. For steady cases, convergence of the numerical solution is indicated by a volume weighted global relative error as proposed by Hou et al. (2013c) for unstructured grids,

$$R(\mathbf{q}) = \sqrt{\frac{\sum_{I}^{N_T}\left[\Omega_{T_i}\left(\frac{\mathbf{q}_{T_i}^{n} - \mathbf{q}_{T_i}^{n-1}}{\mathbf{q}_{T_i}^{n}}\right)^2\right]}{\sum_{I}^{N_T}\Omega_{T_i}}}. \tag{35}$$

If the performance of the model is not satisfactory for a test case, a refinement step will be invoked to prescribe new Manning coefficients according to the flow patterns. By this means, the performance of the new MUSCL scheme based 2D shallow flow model is intensively evaluated through the following test cases.

4.1. Steady flow over uneven bed

Theoretically, a well-balanced scheme is defined to be able to preserve a general moving steady state (Greenberg and Leroux, 1996; Vazquez-Cendon, 1999; Parés and Castro, 2004; Gallardo et al., 2007). But it is common to consider a numerical scheme to be well-balanced even if it only satisfies the C-property of Bermudez and Vazquez (1994), i.e. when the quiescent steady states are preserved (Rebollo et al., 2003; Audusse and Bristeau, 2005; Audusse et al., 2004; Ern et al., 2008; Kim et al., 2008; Delis et al., 2008; Delis and Nikolos, 2013; Nikolos and Delis, 2009; Delis et al., 2011; Liang and Marche, 2009; Liang, 2010; Song et al., 2011b,a; Benkhaldoun et al., 2007, 2010b; Zhou et al., 2001; Xing et al., 2010; Xing and Shu, 2011; Canestrelli et al., 2012, 2010; Pu et al., 2012; Caleffi and Valiani, 2009; Caleffi, 2011). In order to confirm the capability of the present model to converge to a non-stationary steady state (steady flow with non-zero velocities), the steady test case presented in Ricchiuto et al. (2007) and used in Delis et al. (2011) and Delis and Nikolos (2013) is considered in this work.

In this test case, Ricchiuto et al. (2007) consider a solution in which the velocity field is divergence-free and obtained from the harmonic function $\psi = (x - x_0)(y - y_0)$ as:

$$u(x,y) = \frac{\partial \psi}{\partial x} = x - x_0, v(x,y) = \frac{\partial \psi}{\partial y} = -y + y_0, \tag{36}$$

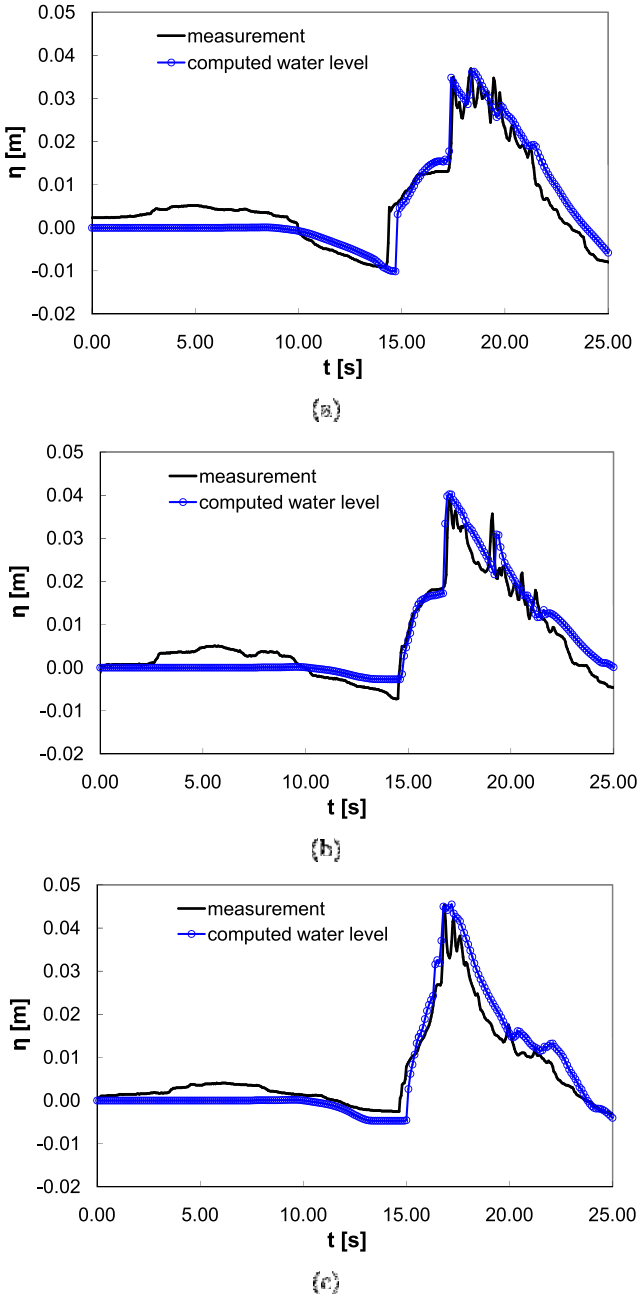

Fig. 32. Tsunami runup onto a complex beach: computed water level history at: (a) G5, (b) G7, (c) G9.

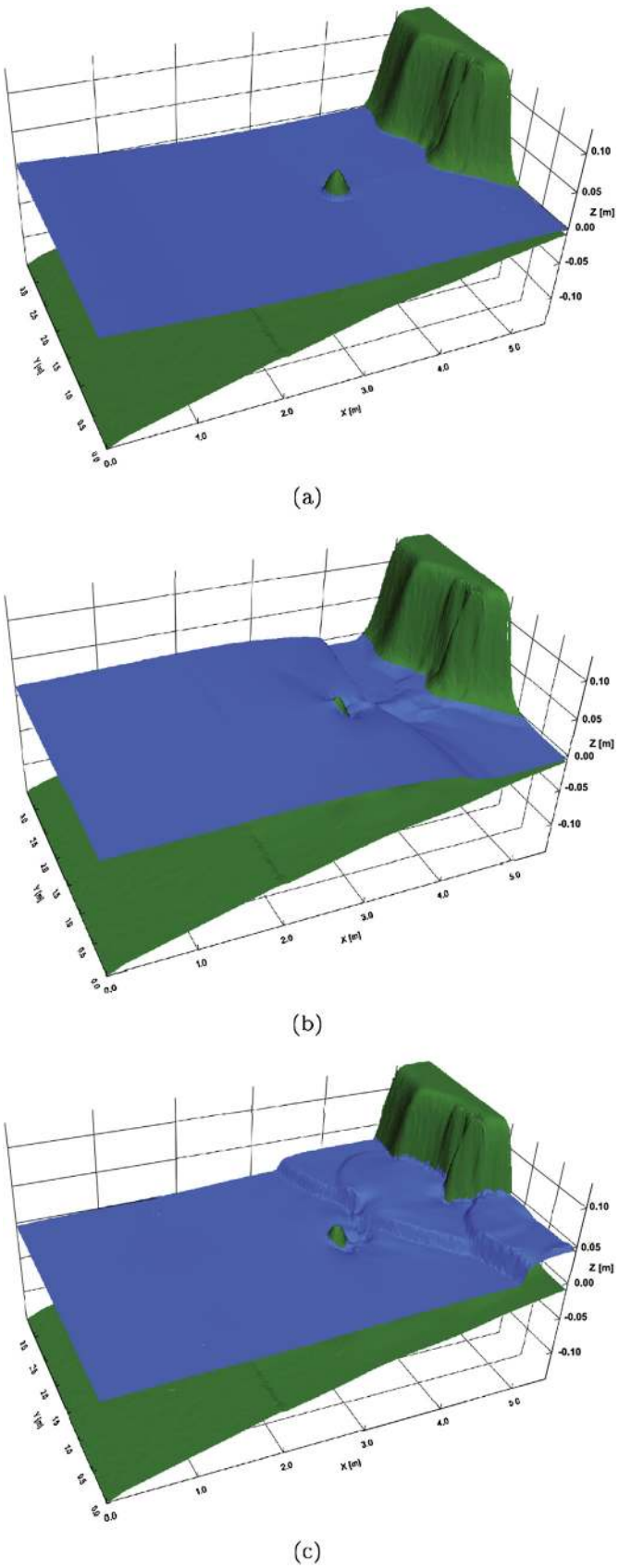

Fig. 33. Tsunami runup onto a complex beach: 3D view of the numerical solution at: (a) $t = 10$ s, (b) $t = 14$ s, (c) $t = 18$ s.

where $[x_0, y_0] = [1, 1]$ denotes the coordinates of the domain center. The bed elevation is given on a 2 m $\times$ 2 m domain with four open boundaries by

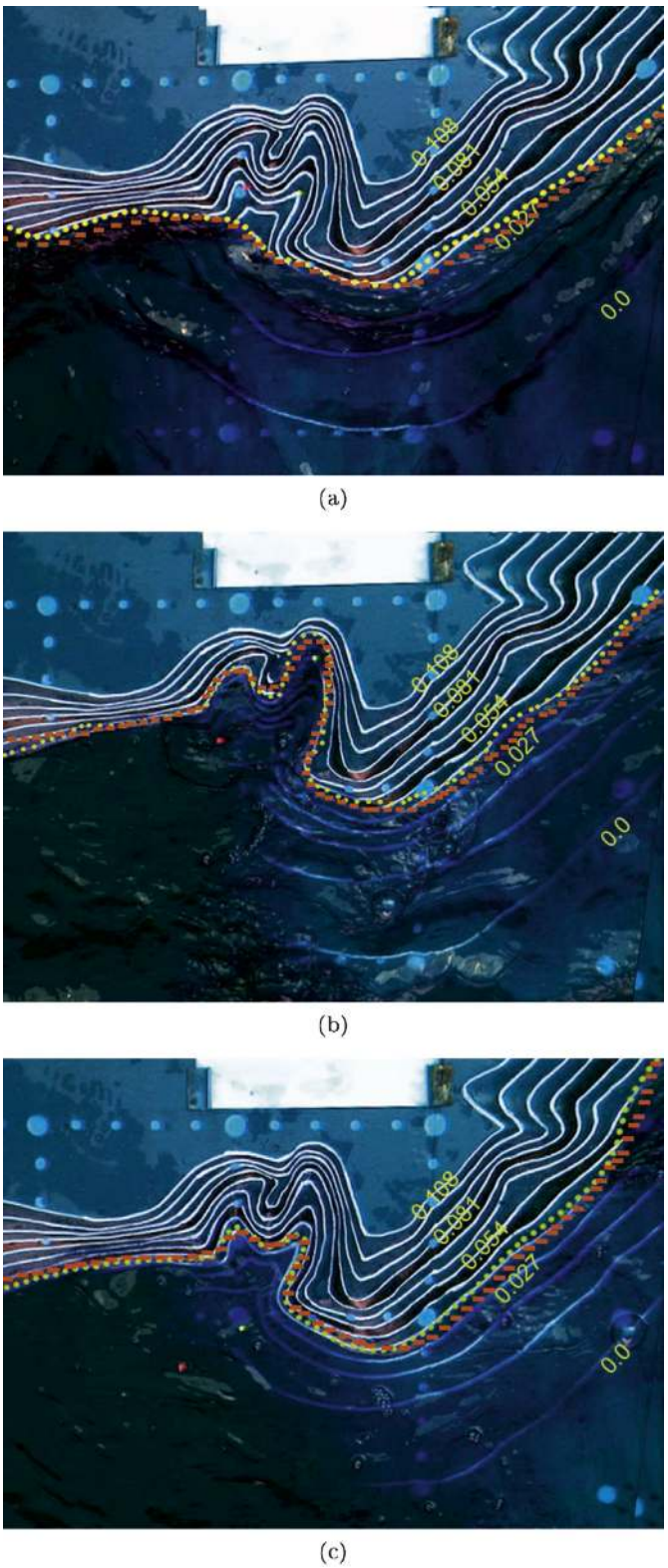

Fig. 34. Tsunami runup onto a complex beach: computed and recorded runup at (a) $t = 15.9$ s, (b) $t = 16.9$ s, (c) $t = 17.9$ s. Computed and recorded wet-dry interfaces are represented by dashed line and dotted line, respectively [m].

$$z_b(x,y) = \frac{1}{g}\left[30 - \frac{|\psi|^2}{2}\right] - \psi - \alpha = \frac{1}{g}\left[30 - \frac{(x-x_0)^2 + (y-y_0)^2}{2}\right] - (x-x_0)(y-y_0) - \alpha, \quad (37)$$

where α=1.5 m and the gravity acceleration $g = 10.0\ \mathrm{ms}^{-2}$ are used. The analytical steady water depth as derived in Ricchiuto et al. (2007) is given by,

$$h(x,y) = \psi + \alpha = (x-x_0)(y-y_0) + \alpha, \quad (38)$$

where the water surface and bed profile are illustrated in Fig. 5.

The current model and the one reported in (Hou et al., 2013a) are run with $\Delta t = 0.005$ s for 6000 iterations on the four different types of commonly used triangular grids with respectively 4066, 5000, 5000 and 4316 cells. These grids are known as the Delaunay grid (type A), Scottish grid (type B), diagonal grid (type C) and distorted grid (type D), respectively (Buffard and Clain, 2010) (Fig. 6). The trend of convergence is reflected by a global relative error $R(h)$ evaluated by Equation (35). The steady state is assumed to be reached when $R(h) < 1 \times 10^{-8}$. As shown in Fig. 7, the new MUSCL scheme can achieve the steady state as defined on all grids and its converging rate is faster than that of the MUSCL scheme of Hou et al. (2013a). In contrast, the previous MUSCL scheme fails to converge on the Scottish grid and the distorted grid, as it is likely to extrapolate improper values at edge midpoints for such a steady case on the grids with distortions and special arrangements of the triangles.

The contours of computed water depth and velocity field on Delaunay grid at $t = 25$ s are respectively presented in Figs. 8 and 9, which are shown to agree closely with the exact solutions. Table 1 compares the relative computational time (with the computational time induced by the new MUSCL scheme on type A grid used as a reference) and the *RRMSE* of the water depth and unit width discharges computed by the two MUSCL schemes on the four grids. The new MUSCL scheme consistently produces favorable results and is able to save around 5% of computational time comparing with the Hou et al. (2013a) scheme.

4.2. Steady flow over frictional uneven bed

This analytical problem was used as a 2D frictional steady state test case in Murillo et al. (2007) and Delis et al. (2011). It is revisited herein to demonstrate the capability of the new MUSCL scheme converging to a steady state with friction effect. When q_x and q_y are given, the analytical solutions of steady-state water depth and bed topography are provided as follows:

$$h(x,y) = 0.5 + xq_x + yq_y, \quad (39)$$

$$z_b(x,y) = -\frac{1}{2g}\frac{\left(q_x^2 + q_y^2\right) + 2gh^3}{h^2} + \frac{3}{7}\frac{n^2 q_x\sqrt{2}}{h^{7/3}}. \quad (40)$$

In this work, a 10 m × 10 m computational domain with the origin defined at the bottom left corner is adopted and the four lateral boundaries are open. Constant q_x and q_y of 0.1 $\mathrm{m^2\ s^{-1}}$ are specified over the whole domain. A high Manning coefficient $n = 0.3\ \mathrm{m^{-1/3}}$ s is used to account for the friction effect. As in Murillo et al. (2007) and Delis et al. (2011), the initial conditions are set to be a flow at rest with water level $\eta = 0.0$ m. The current MUSCL scheme and the one proposed in Hou et al. (2013a) are run with $\Delta t = 0.002$ s for 10,000 iterations on the four types of commonly used triangular grids with respectively 4024, 5000, 5000 and 4403 cells. The steady state is assumed to be achieved if $R(h) < 1 \times 10^{-8}$. Fig. 10 compares the behaviors of the two schemes in terms of convergence rate. The comparison confirms the similar conclusions as in last test case, i.e. the new MUSCL scheme has a higher convergence rate than the MUSCL scheme of Hou et al. (2013a) and is able to reach the defined steady state on all types of grids. The MUSCL scheme of Hou et al. (2013a) is unable to converge on the Scottish grid and the distorted grid, since the scheme fails to extrapolate the right values at the edge midpoints on such grids with distortions and special arrangements of the triangles. In another words, the MUSCL scheme of Hou et al. (2013a) does not meet the generalized well-balanced conditions on the Scottish grid and distorted grid for this test case and this disadvantage is overcome by the new MUSCL scheme.

Figs. 11 and 12 respectively compare the water level and velocities computed at $t = 20$ s by the new MUSCL scheme on the Delaunay grid with exact solutions. Good agreement between the numerical and analytical solutions is observed. Table 2 compares the *RRMSE* computed for the water depth and unit width discharges by the two MUSCL schemes on different grids and demonstrates that the new MUSCL scheme can generally produce better results on all grids. Meanwhile, the new MUSCL scheme is again about 5% more efficient than the original approach as concluded by examining the computational times.

4.3. Circular dam break

As proposed in (Canestrelli et al., 2010), a cylindrical tank of 20 m in diameter is located in the center of the 50 m × 50 m domain with four open boundaries. The tank and the remaining domain are initially filled with 2 m and 0.5 m of still water, respectively. The tank wall is assumed to be removed instantaneously to produce a 2D circular dam-break wave. This process is simulated herein to test the automatic shock-capturing capability of the current model. Again simulations are carried out using the current model and the one presented in Hou et al. (2013a) on four different grids, i.e. the Delaunay grid, Scottish grid, diagonal grid and distorted grid, with respectively 16,024, 16,000, 16,000 and 16,384 cells. Since this is a symmetric test, the 1D solution obtained by the 1D PRICE-C scheme in (Canestrelli et al., 2009) is adopted as a reference to be compared with the 2D numerical solutions.

Fig. 13 shows the 3D view of the computed water level at $t = 1.0$ s and $t = 2.5$ s on the Delaunay grid. Fig. 14 plots the corresponding water levels along the radial direction of $y = 20$ m at $t = 1.0$ s and $t = 2.5$ s. It is apparent that the new MUSCL scheme produces more accurate numerical solution than the first-order upwind scheme (FOU) without inducing spurious oscillations. The new 2D results agree satisfactorily with the 1D reference solutions, demonstrating the capability of the model in resolving 2D shocks. The current numerical solutions also compared well with those presented by Canestrelli et al. (2009) where a 2D unstructured high-order scheme is used and those obtained using the MUSCL scheme as reported in Hou et al. (2013a). A quantitative comparison between the two MUSCL schemes is carried out in Table 3 where low *RRMSE* is observed for the two MUSCL schemes. It indicates that the two schemes actually perform equally well in resolving shocks. However, slight lower *RRMSE* is observed for the new MUSCL scheme especially on the grids of type B and type D. In terms of computational efficiency, the new MUSCL scheme requires approximately 5% less runtime on all grids, comparing with the MUSCL scheme of Hou et al. (2013a).

Numerical diffusion can still be observed for these MUSCL schemes near the shocks as the solution accuracy is locally

switched to become first order to preserve monotonicity (Hirsch, 2007). The shocks can be captured more precisely by refining the grid as shown in Fig. 15, where a Delaunay grid with 49,726 cells is used.

4.4. 2D Riemann problem

Guinot (2003) presented a test case involving a 2D Riemann problem that has been subsequently adopted by other researchers, for example Delis and Nikolos (2013), to test their model's capability in solving complex 2D Riemann problems on unstructured grids. This test case has a 200 m × 200 m frictionless computational domain with [0, 0] defined at the bottom left corner. The Riemann problem is created by imposing discontinuous initial flow conditions as listed in Table 4. The existing (Hou et al., 2013a) and the new MUSCL scheme based models are used to reproduce the complex 2D flow pattern on the aforementioned unstructured girds with 68,712, 80,000, 80,000 and 78,622 cells, respectively. For further comparison, a FOU model is also used in the simulations.

Fig. 16 illustrates the propagation of waves computed by the new MUSCL scheme on the Delaunay grid. The shock wave fronts are well captured by the new MUSCL scheme. The water depth contours and vector fields of the flow velocities on the Delaunay grid are compared respectively in Figs. 17 and 18. Fig. 19 plots the predicted water level across a diagonal section through [0, 0] and [200, 200]. The figures show the computed results of the new MUSCL scheme and that of Hou et al. (2013a) are less diffusive than those obtained from the FOU on different grids. The results of the MUSCL scheme are also observed to be consistent with those reported in Guinot (2003) and Delis and Nikolos (2013). As analytical solution is not available for this test case, further quantitative analysis is not carried out. However, as shown in Fig. 19, particularly in the zoom-in views, the new MUSCL scheme is found to perform slightly better in capturing steeper rarefaction waves. Rarefaction waves are likely to be dampened by low-order schemes, according to the theoretic and numerical analysis reported in Trangenstein (2009) and Toro (2009). From this point of view, the new MUSCL scheme is preferable in modeling shock problems on unstructured grids. The same behavior can also be found on the other three grids. In addition, the new MUSCL scheme could be 4.7%, 5.6%, 5.3% and 6.1% computationally more efficient than the scheme of Hou et al. (2013a) on the four unstructured girds, respectively, further indicating the superiority of the new MUSCL scheme.

4.5. Thacker's planar rotation

The theoretical test case developed in Thacker (1981) is applied herein to demonstrate the accuracy of the present model and its capability in tracking unsteady wet-dry fronts over uneven bed. The planar motion is oscillatory with a small enough amplitude that satisfies the long wave assumption. As the bottom friction is not taken into account, no energy dissipation is involved. This test case has been adopted by many researchers to validate their shallow flow models, for example in Marche et al. (2007), Delis et al. (2008), Ricchiutoa and Bollermann (2009), Song et al. (2011a), Delis and Nikolos (2013) and Hou et al. (2013c). The 2D frictionless parabolic bed topography is defined by

$$z_b(x,y) = -h_0\left[1 - \frac{(x-x_0)^2 + (y-y_0)^2}{a^2}\right], \tag{41}$$

where $[x_0, y_0]$ is the center of the parabolic bowl; h_0 is the water depth at the domain center; a is the distance from the center to the shoreline of zero elevation. The analytical solution to this test case is given by

$$\eta(x,y,t) = \frac{\sigma h_0}{a^2}[2(x-x_0)\cos(\omega t) + 2(y-y_0)\sin(\omega t) - \sigma], \tag{42}$$

$$u(t) = -\omega\sigma\sin(\omega t), \quad v(t) = \omega\sigma\cos(\omega t), \tag{43}$$

in which σ is a constant and $\omega = \sqrt{2gh_0}/a$ is the frequency of the rotation.

In this work, we assume that $h_0 = 0.1$ m, $a = 1.0$ m and $\sigma = 0.5$ m. A 4 m × 4 m computational domain with [0, 0] at the left bottom corner is applied with four solid boundaries. The aforementioned triangular grids of different resolution are again used to test the performance of the new MUSCL scheme (Fig. 6). Simulations are also undertaken using the Hou et al. (2013a) MUSCL scheme for comparison. All of the simulations are run for four rotation periods ($4T$).

The *RMSE* that indicates grid convergence is plotted in Figs. 20–23 for $t = 4T$, where the Δx represents the average cell length for triangular grids and is computed by $\Delta x = \sqrt{\bar{S}}$ and $\bar{S}$ is the averaged cell area. The results demonstrate that the grid convergence rate (order of accuracy) of the new MUSCL scheme is slightly higher than that the existing MUSCL scheme (Hou et al., 2013a), especially on the Scottish grids and the distorted grids. On average, the order of accuracy of the new MUSCL scheme is a range of 1.7–1.75 while that of the existing scheme (Hou et al., 2013a) is between 1.65 and 1.7 for this test. A similar order of accuracy in terms of L_1 errors is also obtained but not presented herein to save space. As expected, the order of accuracy is predicted to be close to but slightly lower than second-order due to the first-order treatment at the wet-dry front; this is a common numerical phenomenon also reported by many other researchers (Bunya et al., 2009; Ricchiuto and A.Bollermann, 2009; Nikolos and Delis, 2009; Delis et al., 2011; Delis and Nikolos, 2013; Hou et al., 2013c). Nevertheless, the solution accuracy is satisfactory for this problem as shown in Fig. 24, which plots the water level and velocities along the cross-section of $y = 2.0$ m at $t = 2.11T$ when the water sloshes at the right hand side, predicted by the present model on the Delaunay grid with 16,000 cells. Good agreement with the analytical water level is observed and the wet-dry fronts are well captured without presenting any numerical instability such as negative water depths. For the velocities, only small discrepancies are detected near the wet-dry fronts where the water depth becomes very small. The similar velocity pattern can also be found for example in Delis et al. (2011). During the simulation, this perturbation does not increase with time and does not affect the predictions of the wet-dry fronts.

In addition, the time history of RMSE of the computed water depth on the Delaunay grid is illustrated in Fig. 25. It indicates again that the new MUSCL scheme performs more favorably against the existing scheme proposed by Hou et al. (2013a). In terms of computational efficiency, the new scheme also consistently performs better and is around 5%–7% more efficient than the existing scheme in all simulations.

4.6. Dam-break flow over a bump

This laboratory test consists of an upstream reservoir filled with 0.111 m of still water and a bump located downstream of the dam (Fig. 26). It is a benchmark test recommended by the EU IMPACT project (IMPACT, 2004) for validating shallow water models in simulating flows with moving wet-dry interface over uneven bed (Hou et al., 2013c, b). The detailed experimental setup and measured data are available in (Soares-Frazão, 2007). In this work, a Delaunay grid with 3960 triangular cells is generated on

the 5.6 m × 0.5 m computational domain with four closed boundaries. Manning coefficient is chosen to be 0.011 $m^{-1/3}$ s as suggested by Soares-Frazão (2007). The simulation is run until $t = 45$ s.

Fig. 27 plots the computed time histories of water level recorded at the three gauges situated along the centerline of the domain at $x = 5.575$ m, $x = 4.925$ m and $x = 3.935$ m (Fig. 26). Fig. 28 shows the computed and measured water levels around the bump. The numerical predictions agree well with the measured data and no numerical instability is detected throughout the simulation. To quantitatively assess the performance of the model, the *RRMSE* of the water level evolution at the three gauges is computed and the values are 5.494%, 8.467% and 7.623%, respectively. For the water level near the bump, the *RRMSE*(η) is evaluated to be 16.813%, 10.146% and 8.842% at $t = 1.8$ s, $t = 3.0$ s and $t = 8.4$ s, respectively. It is verified that the present model with the new MUSCL scheme is acceptable in simulating shallow flows over uneven dry beds on unstructured grids. It should be noted that the computed water level on the right hand side of the bump at $t = 1.8$ s does not fit well with the measurement (Fig. 28a) and the *RRMSE*(η) is about 16.813%. The reason might be because the fully 3D flow features induced by dam-break wave overtopping the bump cannot be accurately captured by a depth-averaged model assuming hydrostatic pressure. Similar predictions can also be found for example in (Hou et al., 2013b). The phenomenon may be also sensitive to bed friction. This is confirmed by the better results, as shown in Fig. 29 and the *RRMSE*(η) of 8.875%, obtained from a further simulation with a reduced Manning coefficient of 0.009 $m^{-1/3}$ s to allow more water overtopping the bump.

4.7. Tsunami runup onto a complex beach

Okushiri island, Japan, was attacked by an earthquake generated tsunami in the Japan Sea in 1993, with a maximum runup of more than 30 m observed at Monai. Following this tsunami event, the Research Institute for Electric Power Industry (CRIEPI) in Abiko, Japan constructed a 1: 400 laboratory model of the area around Monai valley at Okushiri island (Fig. 30) and performed experiments to reproduce the event (Matsuyama and Tanaka, 2001; Liu et al., 2008). This experimental test is considered in this work to verify the capability of the present model with the new MUSCL scheme of simulating long wave propagation onto a complex beach.

The domain and the associated bathymetry used in the experiment are sketched in Fig. 31. The incident tsunami wave created by wave paddles entered the domain with still water through the left open boundary. The full dataset of this test can be downloaded from the website of the NOAA Center for Tsunami Research (Benchmark Methods for Tsunami Model Validation and Verification, 2007). A Delaunay grid consisting of 34,409 triangular cells is used to discretize the problem domain and a constant Manning coefficient of 0.001 $m^{-1/3}$ s is assumed as suggested by other researchers (Popinet, 2011; Funke et al., 2011). Since the measured data for the incoming wave only last for 22.5 s, the simulation is therefore run for $t = 25$ s.

Fig. 33 plots the 3D view of the computed tsunami wave at $t = 10$ s, 14 s and18 s to show the resulting wave propagation. The computed water levels at three gauges (G5, G6 and G7), located at [4.521 m, 1.196 m], [4.521 m, 1.696 m] and [4.521 m, 2.196 m], are compared with the measured data in Fig. 32. In the first 10 s, the water levels cannot be accurately modeled due to existence of initial water disturbances in the wave tank (Zhang and Baptista, 2008; Delis et al., 2008; Nicolsky et al., 2011). Nevertheless, the present model is observed to satisfactorily predict the amplitude and phase of the first wave at all gauges. *RRMSE*(h) is evaluated at the three gauges and the values are 15.991%, 13.715% and 12.951%, respectively. The current numerical results also compare favorably with those reproduced by other unstructured grid based finite volume models, for example in Zhang and Baptista (2008), Cui et al. (2010) and Funke et al. (2011), although a coarser grid is used in the current work. The predicted moving wet-dry interface is also compared with the video records produced by an overhead camera at the frame of 25, 55 and 85 (around t = 15.9 s, 16.9 s and17.9 s), as shown in Fig. 34. Generally good agreement is observed. Furthermore, the maximum runup height is computed to be about 0.083 m, as shown in Fig. 34b at the model scale, which corresponds to 33.2 m at the prototype scale and so agrees well with the field observation.

5. Conclusions

In this paper, a new 2D edge-based MUSCL scheme has been developed on triangular grids to reconstruct the required values at the midpoints of the cell edges in a direct and easy way, by constructing the slopes of variables along the medians of a triangular cell. The new scheme was incorporated into a Godunov-type cell-centered finite volume model as proposed in Hou et al. (2013a,c,b) for solving the SWEs.

Extensive numerical experiments suggest that the SWE model implemented with the novel MUSCL scheme is able to converge to steady state, capture shocks and handle complex shallow flows involving wetting and drying over complex beds. Comparing with the existing approach recently reported in Hou et al. (2013a), the current MUSCL scheme has a slightly higher accuracy for general shallow flow solutions, and offers a better well-balanced property indicated by a faster convergent rate to steady solutions on different triangular girds. Furthermore, the novel MUSCL scheme is able to save around 5% of the computational time comparing with the previous model presented by Hou et al. (2013a). The new scheme is also flexible and easy to be implemented on all triangular grids. As a summary, due to its better solution accuracy, higher computational efficiency and simplicity, the proposed MUSCL scheme provides a favorable alternative to the existing approaches for solving the SWEs. It can also be directly extended to solve other hyperbolic equations, e.g. the advection–diffusion equation which is widely used in environmental flow simulations. In addition, the scheme, presented here for the 2D triangular grids, can be easily generalized into 3D tetrahedron grids for solving the 3D problems.

Acknowledgment

This work is funded by the UK Engineering and Physical Sciences Research Council (EPSRC) project 'Flood MEMORY: Multi-Event Modelling Of Risk & recoverY' (EP/K013513/1) and the UK Natural Environment Research Council (NERC) project 'SINATRA: Susceptibility of catchments to INTense RAinfall and flooding' (NE/K008781/1).

References

Aftosmis, M., Gaitonde, D., Tavares, T., 1994. On the Accuracy, Stability and Monotonicity of Various Reconstruction Algorithms for Unstructured Meshes. AIAA paper 94–0415.

Aftosmis, M., Gaitonde, D., Tavares, T., 1995. Behavior of linear reconstruction techniques on unstructured meshes. AIAA J. 33, 2038–2049.

Akbar, M., Aliabadi, S., 2013. Hybrid numerical methods to solve shallow water equations for hurricane induced storm surge modeling. Environ. Model. Softw. 46, 118–128.

Anastasiou, K., Chan, C., 1997. Solution of the 2D shallow water equations using the finite volume method on unstructured grids. Int. J. Numer. Methods Fluids 24, 1225–1245.

Ani, E.-C., Wallis, S., Kraslawski, A., Agachi, P.S., Oct 2009. Development,calibration and evaluation of two mathematical models for pollutant transport in a small river. Environ. Model. Softw. 24 (10), 1139–1152.
Audusse, E., Bouchut, F., Bristeau, M.-O., Klein, R., Perthame, B., 2004. A fast and stable well-balanced scheme with hydrostatic reconstruction for shallow water flows. SIAM J. Sci. Comput. 25, 2050–2065.
Audusse, E., Bristeau, M.O., 2005. A well-balanced positivity preserving second-order scheme for shallow water flows on unstructured meshes. J. Comput. Phys. 206, 311–333.
Barth, T.J., Jespersen, D.C., 1989. The Design and Application of Upwind Schemes on Unstructured Meshes, pp. 1–12. AIAA Paper 89-0366.
Begnudelli, L., Sanders, B.F., 2006. Unstructured grid finite-volume algorithm for shallow-water flow and scalar transport with wetting and drying. J. Hydraul. Eng. 132, 371–384.
Begnudelli, L., Sanders, B.F., 2007. Conservative wetting and drying methodology for quadrilateral grid finite-volume models. J. Hydraul. Eng. 133, 312–322.
Begnudelli, L., Sanders, B.F., Bradford, S.F., 2008. Adaptive Godunov-Based model for flood simulation. J. Hydraul. Eng. 134, 714–725.
Benchmark Methods for Tsunami Model Validation and Verification, 2007. Noaa Center for Tsunami Research. URL http://nctr.pmel.noaa.gov.
Benkhaldoun, F., Elmahi, I., Seaid, M., 2007. Well-balanced finite volume schemes for pollutant transport by shallow water equations on unstructured meshes. J. Comput. Phys. 226, 180–203.
Benkhaldoun, F., Elmahi, I., Seaid, M., 2010a. A new finite volume method for flux-gradient and source-term balancing in shallow water equations. Comput. Methods Appl. Mech. Eng. 3324–3335.
Benkhaldoun, F., Sahmim, S., Seaid, M., 2010b. A two-dimensional finite volume morphodynamic model on unstructured triangular grids. Int. J. Numer. Methods Fluids 63, 1296–1327.
Bennett, N.D., Croke, B.F., Guariso, G., Guillaume, J.H., Hamilton, S.H., Jakeman, A.J., Marsili-Libelli, S., Newham, L.T., Norton, J.P., Perrin, C., et al., Feb 2013. Characterising performance of environmental models. Environ. Model. Softw. 40, 1–20.
Bermudez, A., Vazquez, M.E., 1994. Upwind methods for hyperbolic conservation laws with source terms. Comput. Fluids 23, 1049–1071.
Bradford, S.F., Sanders, B.F., 2002. Finite-volume model for shallow-water flooding of arbitrary topography. J. Hydraul. Eng. 128, 289–298.
Bradford, S.F., Sanders, B.F., 2005. Performance of high resolution, non-level bed, shallow-water models. J. Hydraul. Eng. 131, 1073–1081.
Brufau, P., Garcia-Navarro, P., Vazquez-Cendon, M.E., 2004. Zero mass error using unsteady wetting-drying conditions in shallow flows over dry irregular topography. Int. J. Numer. Methods Fluids 45, 1047–1082.
Buffard, T., Clain, S., 2010. Monoslope and multislope MUSCL methods for unstructured meshes. J. Comput. Phys. 229, 3745–3776.
Bunya, S., Kubatko, E.J., Westerink, J.J., Dawson, C., 2009. A wetting and drying treatment for the Runge-Kutta discontinuous Galerkin solution to the shallow water equations. Comput. Methods Appl. Mech. Eng. 198, 1548–1562.
Bussing, T.R., Murmant, E.M., 1988. Finite-volume method for the calculation of compressible chemically reacting flows. AIAA J. 26, 1070–1078.
Caleffi, V., 2011. A new well-balanced hermite weighted essentially non-oscillatory scheme for shallow water equations. Int. J. Numer. Methods Fluids 67, 1135–1159.
Caleffi, V., Valiani, A., 2009. Well-balanced bottom discontinuities treatment for high-order shallow water equations WENO scheme. J. Eng. Mech. 135, 684–696.
Canestrelli, A., Dumbser, M., Siviglia, A., Toro, E.F., 2010. Well-balanced high-order centered schemes on unstructured meshes for shallow water equations with fixed and mobile bed. Adv. Water Resour. 33, 291–303.
Canestrelli, A., Fagherazzi, S., Lanzoni, S., 2012. A mass-conservative centered finite volume model for solving two-dimensional two-layer shallow water equations for fluid mud propagation over varying topography and dry areas. Adv. Water Resour. 40, 54–70.
Canestrelli, A., Siviglia, A., Dumbser, M., Toro, E.F., 2009. Well-balanced high-order centred schemes for non-conservative hyperbolic systems. applications to shallow water equations with fixed and mobile bed. Adv. Water Resour. 32, 834–844.
Cao, Z., Pender, G., Carling, P., 2006. Shallow water hydrodynamic models for hyperconcentrated sediment-laden floods over erodible bed. Adv. Water Resour. 29 (4), 546–557.
Chippada, S., Dawson, C., Martinez, M., Wheeler, M., 1998. A Godunov type finite volume method for the system of shallow water equations. Comput. Methods Appl. Mech. Eng. 151, 105–129.
Cui, H., Pietrzak, J., Stelling, G., 2010. A finite volume analogue of the finite element: with accurate flooding and drying. Ocean. Model. 35 (1), 16–30.
Delis, A., Nikolos, I., 2013. A novel multidimensional solution reconstruction and edge-based limiting procedure for unstructured cell-centered finite volumes with application to shallow water dynamics. Int. J. Numer. Methods Fluids 71, 584–633.
Delis, A., Nikolos, I., Kazolea, M., 2011. Performance and comparison of cell-centered and node-centered unstructured finite volume discretizations for shallow water free surface flows. Arch. Comput. Methods Eng. 18, 57–118.
Delis, A.I., Kazolea, M., Kampanis, N.A., 2008. A robust high-resolution finite volume scheme for the simulation of long waves over complex domains. Int. J. Numer. Methods Fluids 56, 419–452.
Ern, A., Piperno, S., Djadel, K., 2008. A well-balanced Runge-Kutta discontinuous Galerkin method for the shallow-water equations with flooding and drying. Int. J. Numer. Methods Fluids 58, 1–25.
Esteves, M., Faucher, X., Galle, S., Esteves, M., 2000. Overland flow and infiltration modelling for small plots during unsteady rain: numerical results versus observed values. J. Hydrol. 228 (3), 265–282.
Frink, N.T., 1991. Upwind scheme for solving the Euler equations on unstructured tetrahedral meshes. AIAA J. 30, 70–77.
Funke, S., Pain, C., Kramer, S., Piggott, M., 2011. A wetting and drying algorithm with a combined pressure/free-surface formulation for non-hydrostatic models. Adv. Water Resour. 34, 1483–1495.
Gallardo, J.M., Pares, C., Castro, M., 2007. On a well-balanced high-order finite volume scheme for shallow water equations with topography and dry areas. J. Comput. Phys. 227, 574–601.
George, D.L., 2010. Adaptive finite volume methods with well-balanced riemann solvers for modeling floods in rugged terrain: application to the malpasset dam-break flood (France, 1959). Int. J. Numer. Methods Fluids 66, 1000–1018.
Gomez, M., Tchijov, V., Apr 2010. The FEOM technique applied to a three-dimensional model of diffusion/advection of pollutants. Environ. Model. Softw. 25 (4), 602–606.
Greenberg, J., Leroux, A., 1996. A well-balanced scheme for the numerical processing of source terms in hyperbolic equations. SIAM J. Numer. Anal. 33, 1–16.
Guinot, V., 2003. Godunov-type Schemes: an Introduction for Engineers. Elsevier.
Hinkelmann, R., 2005. Efficient Numerical Methods and Information-processing Techniques for Modeling Hydro- and Environmental Systems. Springer.
Hirsch, C., 2007. Numerical Computation of Internal and External Flows, second ed. Elsevier.
Hou, J., Liang, Q., Simons, F., Hinkelmann, R., 2013a. A 2D well-balanced shallow flow model for unstructured grids with novel slope source term treatment. Adv. Water Resour. 52, 107–131.
Hou, J., Liang, Q., Simons, F., Hinkelmann, R., 2013b. A stable 2D unstructured shallow flow model for simulations of wetting and drying over rough terrains. Comput. Fluids 82, 132–147.
Hou, J., Simons, F., Mahgoub, M., Hinkelmann, R., 2013c. A robust well-balanced model on unstructured grids for shallow water flows with wetting and drying over complex topography. Comput. Methods Appl. Mech. Eng. 257, 126–149.
Hubbard, M., 1999. Multidimensional slope limiters for MUSCL-type finite volume schemes on unstructured grids. J. Comput. Phys. 155, 54–74.
Hunter, N.M., Bates, P.D., Horritt, M.S., Wilson, M.D., 2007. Simple spatially-distributed models for predicting flood inundation: a review. Geomorphology 90 (3), 208–225.
IMPACT, 2004. Investigation of Extreme Flood Processes and Uncertainties. Ec contract evg1-ct-2001–00037. URL. www.impact-project.net.
Jawahar, P., Kamath, H., 2000. A high-resolution procedure for Euler and Navier-Stokes computations on unstructured grids. J. Comput. Phys. 164, 165–203.
Kim, D.-H., Cho, Y.-S., Kim, H.-J., 2008. Well-balanced scheme between flux and source terms for computation of shallow-water equations over irregular bathymetry. J. Hydraul. Eng. 134, 277–290.
Kneis, D., Förster, S., Bronstert, A., 2009. Simulation of water quality in a flood detention area using models of different spatial discretization. Ecol. Model. 220 (13), 1631–1642.
Kong, J., Xin, P., Shen, C.-J., Song, Z.-Y., Li, L., 2013. A high-resolution method for the depth-integrated solute transport equation based on an unstructured mesh. Environ. Model. Softw. 40, 109–127.
Kourakos, G., Harter, T., Feb 2014. Vectorized simulation of groundwater flow and streamline transport. Environ. Model. Softw. 52, 207–221.
Kuiry, S.N., Pramanik, K., Sen, D., 2008. Finite volume model for shallow water equations with improved treatment of source terms. J. Hydraul. Eng. 134, 231–242.
La Rocca, M., Adduce, C., Sciortino, G., Pinzon, A.B., 2008. Experimental and numerical simulation of three-dimensional gravity currents on smooth and rough bottom. Phys. Fluids 20 (10), 106603.
Liang, D., Wang, X., Falconer, R.A., Bockelmann-Evans, B.N., Dec 2010. Solving the depth-integrated solute transport equation with a TVD-maccormack scheme. Environ. Model. Softw. 25 (12), 1619–1629.
Liang, Q., 2010. flood simulation using a well-balanced shallow flow model. J. Hydraul. Eng. 136, 669–675.
Liang, Q., Borthwick, A.G., 2009. Adaptive quadtree simulation of shallow flows with wet dry fronts over complex topography. Comput. Fluids 38, 221–234.
Liang, Q., Marche, F., 2009. Numerical resolution of well-balanced shallow water equations with complex source terms. Adv. Water Resour. 32, 873–884.
Liu, P.L.-F., Yeh, H., Synolakis, C. (Eds.), 2008. Advanced Numerical Models for Simulating Tsunami Waves and Runup. World Scientific Pub. Co., Inc.
Liu, X.-D., Jun 1993. A maximum principle satisfying modification of triangle based adapative stencils for the solution of scalar hyperbolic conservation laws. SIAM J. Numer. Anal. 30 (3), 701–716.
Loukili, Y., Soulaimani, A., 2007. Numerical tracking of shallow water waves by the unstructured finite volume WAF approximation. Int. J. Comput. Methods Eng. Sci. Mech. 8, 1–14.
Marche, F., Bonneton, P., Fabrie, P., Seguin, N., 2007. Evaluation of well-balanced bore-capturing schemes for 2D wetting and drying processes. Int. J. Numer. Methods Fluids 53, 867–894.
Matsuyama, M., Tanaka, H., 2001. An experimental study of the highest run-up height in 1993 Hokkaido Nansei-oki earthquake tsunami. In: Proceedings of the International Tsunami Symposium. Seattle, U.S.A.
Murillo, J., Garcia-Navarro, P., 2011. Improved riemann solvers for complex transport in two-dimensional unsteady shallow flow. J. Comput. Phys. 230, 7202–7239.

Murillo, J., Garcia-Navarro, P., Burguete, J., 2008. Analysis of a second-order upwind method for the simulation of solute transport in 2D shallow water flow. Int. J. Numer. Methods Fluids 56, 661–686.
Murillo, J., Garcia-Navarro, P., Burguete, J., 2009. Conservative numerical simulation of multi-component transport in two-dimensional unsteady shallow water flow. J. Comput. Phys. 228, 5539–5573.
Murillo, J., Garcia-Navarro, P., Burguete, J., Brufau, P., 2006. A conservative 2D model of inundation flow with solute transport over dry bed. Int. J. Numer. Methods Fluids 52, 1059–1092.
Murillo, J., Garcia-Navarro, P., Burguete, J., Brufau, P., Jun 2007. The influence of source terms on stability, accuracy and conservation in two-dimensional shallow flow simulation using triangular finite volumes. Int. J. Numer. Methods Fluids 54 (5), 543–590.
Nicolsky, D., Suleimani, E., Hansen, R., 2011. Validation and verification of a numerical model for tsunami propagation and runup. Pure Appl. Geophys. 168, 1199–1222.
Nikolos, I., Delis, A., 2009. An unstructured node-centered finite volume scheme for shallow water flows with wet/dry fronts over complex topography. Comput. Methods Appl. Mech. Eng. 198, 3723–3750.
Parés, C., Castro, M., 2004. On the well-balance property of Roe's method for nonconservative hyperbolic systems. Applications to shallow-water systems. ESAIM: Math. Model. Numer. Anal. 38, 821–852.
Park, J.S., Yoon, S.-H., Kim, C., 2010. Multi-dimensional limiting process for hyperbolic conservation laws on unstructured grids. J. Comput. Phys. 229, 788–812.
Pelling, H.E., Green, J.M., Ward, S.L., 2013. Modelling tides and sea-level rise: to flood or not to flood. Ocean. Model. 63, 21–29.
Popinet, S., 2011. Quadtree-adaptive tsunami modelling. Ocean. Dyn. 61, 1261–1285.
Pu, J.H., Cheng, N.-S., Tan, S.K., Shao, S., 2012. Source term treatment of SWEs using surface gradient upwind method. J. Hydraul. Res. 50, 145–153.
Rebollo, T.C., Delgado, A.D., Nieto, E.D.F., 2003. A family of stable numerical solvers for the shallow water equations with source terms. Comput. Methods Appl. Mech. Eng. 192, 203–225.
Ricchiuto, M., Abgrall, R., Deconinck, H., 2007. Application of conservative residual distribution schemes to the solution of the shallow water equations on unstructured meshes. J. Comput. Phys. 222 (1), 287–331.
Ricchiuto, M., Bollermann, A., 2009. Accuracy of stabilized residual distribution for shallow water flows including dry beds. In: Tadmor, E., Liu, J.G., Tzavaras, A. (Eds.), HYP08: Proceedings of the 12th International Conference on Hyperbolic Problems: Theory, Numerics, Applications. AMS Proc. Symp. Appl. Math. 67 (2).
Ricchiutoa, M., Bollermann, A., 2009. Stabilized residual distribution for shallow water simulations. J. Comput. Phys. 228, 1071–1115.
Rubio, A., Zalts, A., El Hasi, C., Jan 2008. Numerical solution of the advection–reaction–diffusion equation at different scales. Environ. Model. Softw. 23 (1), 90–95.
Sanders, B.F., Schubert, J.E., Detwiler, R.L., 2010. Parbrezo: a parallel, unstructured grid, Godunov-type, shallow next term-previous term water next term code for high-resolution flood inundation modeling at the regional scale. Adv. Water Resour. 33, 1456–1467.
Simões, F.J., 2011. Finite volume model for two-dimensional shallow environmental flow. J. Hydraul. Eng. 137 (2), 173–182.
Simons, F., Busse, T., Hou, J., Notay, K., Hinkelmann, R., 2011. A robust and efficient solver for the shallow water equations and its application to a complex natural hydrosystem. In: Proceedings of the 34th IAHR Congress. Brisbane, Australia, pp. 4276–4283.
Simons, F., Busse, T., Hou, J., Ozgen, I., Hinkelmann, R., 2014. A model for overland flow and associated processes within the hydroinformatics modelling system. J. Hydroinform. 16 (2), 375–391.
Skoula, Z., Borthwick, A., Moutzouris, C., 2006. Godunov-type solution of the shallow water equations on adaptive unstructured triangular grids. Int. J. Comput. Fluid Dyn. 20, 621–636.
Soares-Frazão, S., 2007. Experiments of dam-break wave over a triangular bottom sill. J. Hydraul. Res. 45, 19–26.
Song, L., Zhou, J., Guo, J., Zou, Q., Liu, Y., 2011a. A robust well-balanced finite volume model for shallow water flows with wetting and drying over irregular terrain. Adv. Water Resour. 34, 915–932.
Song, L., Zhou, J., Li, Q., Yang, X., Zhang, Y., 2011b. An unstructured finite volume model for dam-break floods with wet/dry fronts over complex topography. Int. J. Numer. Methods Fluids 67, 960–980.
Sugawara, D., Goto, K., 2012. Numerical modeling of the 2011 Tohoku-oki tsunami in the offshore and onshore of Sendai plain, Japan. Sediment. Geol. 282, 110–123.
Sun, M., Takayama, K., 2003. Error localization in solution-adaptive grid methods. J. Comput. Phys. 190, 346–350.
Thacker, W.C., 1981. Some exact solutions to the nonlinear shallow-water wave equations. J. Fluid Mech. 107, 499–508.
Toro, E., Spruce, M., Speares, W., 1994. Restoration of the contact surface in the HLL-Riemann solver. Shock Waves 4, 25–34.
Toro, E.F., 2009. Riemann Solvers and Numerical Methods for Fluid Dynamics a Practical Introduction, third ed. Springer-Verlag, Berlin Heidelberg.
Trangenstein, J.A., 2009. Numerical Solution of Hyperbolic Partial Differential Equations. Cambridge University Press.
van Albada, G., van Leer, B., Roberts, W., 1982. A comparative study of computational methods in cosmic gas dynamics. Astron. Astrophys. 108, 76–84.
van Leer, B., 1979. Towards the ultimate conservative difference scheme. V. A second-order sequel to Godunov's method. J. Comput. Phys. 32, 101–136.
Vazquez-Cendon, M.E., 1999. Improved treatment of source terms in upwind schemes for the shallow water equations in channels with irregular geometry. J. Comput. Phys. 148, 497–526.
Venkatakrishnan, V., 1995. Convergence to steady state solutions of the Euler equations on unstructured grids with limiters. J. Comput. Phys. 118, 120–130.
Venkatakrishnan, V., Allmaras, S., Kamenetskii, D., Johnson, F., 2003. Higher Order Schemes for the Compressible Navier-Stokes Equations, pp. 1–17. AIAA Paper 03-3987.
Viero, D.P., Alpaos, A.D., Carniello, L., Alpaos, A.D., 2013. Mathematical modeling of flooding due to river bank failure. Adv. Water Resour. 59, 82–94.
Wang, Y., Liang, Q., Kesserwani, G., Hall, J.W., 2011. A 2D shallow flow model for practical dam-break simulations. J. Hydraul. Res. 49, 307–316.
Xing, Y., Shu, C.-W., 2011. High-order finite volume WENO schemes for the shallow water equations with dry states. Adv. Water Resour. 34, 1026–1038.
Xing, Y., Zhang, X., Shu, C.-W., 2010. Positivity-preserving high order well-balanced discontinuous Galerkin methods for the shallow water equations. Adv. Water Resour. 33, 1476–1493.
Yoon, T.H., Kang, S.-K., 2004. Finite volume model for two-dimensional shallow water flows on unstructured grids. J. Hydraul. Eng. 130, 678–688.
Zhang, Y.J., Baptista, A.M., 2008. An efficient and robust tsunami model on unstructured grids. Part I: Inundation benchmarks. Pure Appl. Geophys. 165 (11–12), 2229–2248.
Zhou, J., Causon, D., Mingham, C., Ingram, D., 2001. The surface gradient method for the treatment of source terms in the shallow-water equations. J. Comput. Phys. 168, 1–25.
Zhou, J., Causon, D., Mingham, C., Ingram, D., 2004. Numerical prediction of dam-break flows in general geometries with complex bed topography. J. Hydraul. Eng. 130, 332–340.
Zokagoa, J.M., Soulaimani, A., 2010. Modeling of wetting-drying transitions in free surface flows over complex topographies. Comput. Methods Appl. Mech. Eng. 199, 2281–2304.